International Journal of Fatigue 132 (2020) 105363

Contents lists available at ScienceDirect

International Journal of Fatigue

journal homepage: www.elsevier.com/locate/ijfatigue

Fatigue of additive manufactured Ti-6Al-4V, Part II: The relationship between microstructure, material cyclic properties, and component performance

R. Molaei[a], A. Fatemi[a,b,*], N. Sanaei[b], J. Pegues[c,d], N. Shamsaei[c,d], S. Shao[c,d], P. Li[e], D.H. Warner[e], N. Phan[f]

[a] Mechanical Engineering, University of Memphis, Memphis, TN 38152, USA
[b] Mechanical, Industrial and Manufacturing Engineering, University of Toledo, Toledo, OH 43606, USA
[c] Mechanical Engineering, Auburn University, Auburn, AL 36849, USA
[d] National Center for Additive Manufacturing Excellence (NCAME), Auburn University, Auburn, AL 36849, USA
[e] Cornell Fracture Group, School of Civil and Environmental Engineering, Cornell University, Ithaca, NY 14853, USA
[f] Structures Division, U.S. Naval Air Systems Command (NAVAIR), Patuxent River, MD 20670, USA

ARTICLE INFO

Keywords:
Additive manufacturing
Powder Bed Fusion (PBF)
Ti-6Al-4V
Fatigue behavior
Multiaxial stresses

ABSTRACT

Part I of these two-part paper series focused on the process and structure relationships, effect of powder feedstock, fabrication parameters, and post fabrication treatments on the resulting microstructure, defect characteristics, and surface quality of the fabricated Ti-6Al-4V parts. This second part extends the study by evaluating the effect of the aforementioned factors on axial, torsion, and multiaxial fatigue behavior of the additively manufactured (AM) Ti-6Al-4V specimens. Despite the advantages of additive manufacturing techniques discussed in Part I, they are still rarely used in fatigue critical load carrying applications, partly due to insufficient understanding of fatigue behavior and its dependence on variations in material microstructure and defects. This becomes even more challenging when other process characteristics of AM including build orientation, residual stresses, and surface roughness are considered. This paper discusses these effects, as well as machine-to-machine variability and the effects of specimen geometry and size, post heat treatment, and multiaxial stress state. Experimental uniaxial, torsion, and multiaxial fatigue test results recently generated by the authors for laser beam powder bed fusion- produced Ti-6Al-4V alloy are reviewed. The observed behaviors and the influence of the aforementioned effects are then related to the resulting microstructure and defect characteristics discussed in Part I. Fatigue life prediction results for specimens based on the effective defect size calculated by extreme value statistics (EVS) of the internal defects and surface roughness are also presented and compared with experimental data. The observed behaviors and specimen test results are then used for fatigue life analysis and predictions of a link component as an illustrative application example.

1. Introduction

In the first part of this two-part publication, the effects of powder feedstock, fabrication parameters, and post manufacturing treatments on the resulting microstructure, defect characteristics, and surface quality were discussed. This second part evaluates the effects of the aforementioned factors on the fatigue behavior of Additively Manufactured (AM) Ti-6Al-4V alloy. Despite the advantages of Additive Manufacturing (AM) discussed in Part I [1], this technology is still not used in critical load carrying applications, partly due to insufficient understanding of cyclic deformation and fatigue behavior. Fatigue behavior varies with microstructure, intrinsic internal defects, residual stresses, and surface roughness, which in turn depend on the process parameters and post treatments used.

Fatigue cracks generally initiate from defects such as inclusions, internal pores, and surface roughness, or within the regions where a number of adjacent grains of nearly the same orientation have the slip characteristics of a single large grain [2]. This becomes more important for AM metals where defects and uncertainties in microstructural characteristics are key concerns. As discussed in Part I [1], this uncertainty arises from a vast number of parameters including build methods and procedures, AM systems, process parameters, feedstock

* Corresponding author at: Mechanical Engineering, University of Memphis, Memphis, TN 38152, USA.
E-mail address: afatemi@memphis.edu (A. Fatemi).

https://doi.org/10.1016/j.ijfatigue.2019.105363
Received 30 August 2019; Received in revised form 30 October 2019; Accepted 1 November 2019
Available online 04 November 2019
0142-1123/

Nomenclature

a	crack length
b	fatigue strength exponent
C	paris equation coefficient
C'	constant in modified Paris equation
da/dN	crack propagation rate
G	shear Young's modulus
k	constant in Fatemi-Socie parameter
n	Paris equation exponent
$2N_f$	reversals to failure
R	minimum to maximum stress or strain ratio
R_a	arithmetic mean of surface roughness
R_t	max peak-to-valley roughness
R_{zISO}	10-point height roughness
α	maximum principal stress angle
γ_a	shear strain amplitude
ε_a	axial strain amplitude
$\bar{\varepsilon}_a$	von-Mises effective strain amplitude
$\bar{\rho}$	10-point valley radius
σ_a	axial stress amplitude
σ_{eff}	effective stress
σ_{max}	maximum stress
$\bar{\sigma}_a$	von-Mises equivalent stress amplitude
$\bar{\sigma}_{1a}$	maximum principal stress amplitude
σ'_f	fatigue strength coefficient
τ_a	shear stress amplitude
$\sqrt{area_{D,max}}$	maximum prospective internal defect size
$\sqrt{area_{eff}}$	effective defect size
$\sqrt{area_P}$	projection of the effective maximum prospective defect size
$\sqrt{area_{R,max}}$	maximum prospective equivalent surface defect size from roughness profile

Abbreviations

AM	Additive Manufacturing/Additively Manufactured
BCC	Body Center Cubic
CIS	Crack Initiation Site
DED	Directed Energy Deposition
E-Beam PBF	Electron-Beam Powder Bed Fusion
EBSD	Electron Backscatter Diffraction
EVS	Extreme Value Statistics
FCC	Face Centered Cubic
FEA	Finite Element Analysis
FS	Fatemi-Socie Damage Parameter
HCF	High Cycle Fatigue
HCP	Hexagonal Close Packed
HIP	Hot Isostatic Pressing
LCF	Low Cycle Fatigue
LOF	Lack of Fusion
LB-PBF	Laser Beam Powder Bed Fusion
PBF	Powder Bed Fusion
TCD	Theory of Critical Distance
TIG	Tungsten Inert Gas Torch Wire-Feed DED
VHCF	Very High Cycle Fatigue

characteristics, and post manufacturing treatments. These variations, in turn, affect the microstructural details (such as grain size, morphology, and texture), defect characteristics (such as size, shape, location, and density), and residual stresses and, therefore, mechanical behavior in general, and fatigue performance in particular.

It is often desirable to determine the mechanical performance of a component from simple monotonic tensile test results. Tensile tests are easy and inexpensive to perform, as compared to fatigue tests, which are time consuming and more complicated. However, since the majority of components undergo cyclic loading throughout their service life, fatigue properties of the materials are of utmost importance to their design [3]. Over the years, several methods have been proposed to develop correlations amongst the monotonic tensile data and fatigue properties of conventional materials, for example in [4,5]. Nevertheless, since fatigue behavior is much more sensitive than tensile behavior to the characteristics of microstructure and defects, it is difficult to develop a robust relationship between tensile and fatigue properties.

Fig. 1 shows correlation of the ultimate tensile strength versus fatigue limit (defined as fatigue strength at 10^7 cycles) from several studies for Ti-6Al-4V manufactured by different AM techniques with different post heat treatment conditions, for two different stress ratios commonly used to generate fatigue data [6–21]. It is worth mentioning that when there was not a data point at 10^7 cycles, the fatigue limit was estimated using a power law fit of the reported stress versus life data. As can be seen, there is a lack of correlation between monotonic tensile and fatigue strength across various AM techniques, as well as within particular fabrication methods, i.e. PBF data with different heat treatments.

An extensive review of published AM Ti-6Al-4V fatigue data was conducted in [22]. The review included a comprehensive analysis of different aspects of this alloy, including microstructure, failure mechanisms, processing parameters, and defects. Among the fatigue data sets examined, none matched the performance of wrought Ti-6Al-4V material without a post build surface treatment. Further, only the TIG wire-feed Directed Energy Deposition (DED) method was shown to

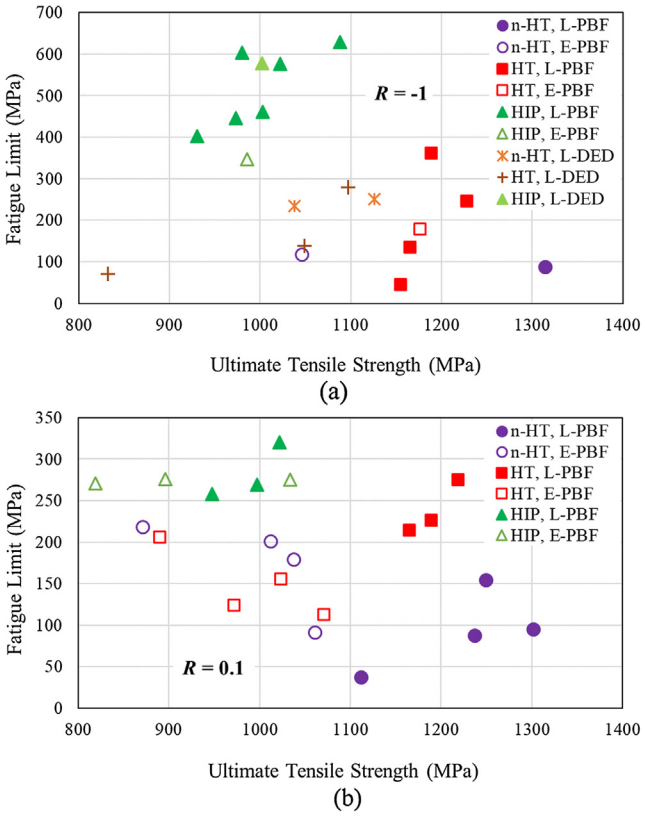

Fig. 1. Correlation of fatigue limit defined as fatigue strength at 10^7 cycles with monotonic ultimate tensile strength for AM Ti-6Al-4V for (a) $R = -1$, and (b) $R = 0.1$ stress ratios. The data were extracted from several available studies in the literature. The data are divided to n-HT (as-built non-heat treated), HT (annealed and/or heat treated), and HIPed categories.

exhibit performance comparable to wrought material without post fabrication heat treatment. In closing, the review points out the possibility that further advancement of AM technology, e.g. optimization of build parameters and improvements in the feedstock material, might soon provide near wrought fatigue performance without these expensive post processing steps.

This paper, as the second part of a series, mostly contains recent experimental fatigue data generated by the authors in a collaborative effort on Laser Beam Powder Bed Fusion (LB-PBF) Ti-6Al-4V alloy. Fatigue performance of the fabricated specimens with two different fabrication machines and different geometries are reviewed for axial, torsion, and combined axial-torsion loading conditions. Details regarding the associated fabrication processes, sample geometries and heat treatment are discussed in Section 2. Torsion or multiaxial loads are discussed, which are common for many components and structural members. Even in parts under uniaxial loading conditions, the stress state may be biaxial or multiaxial due to complex geometries, residual stresses, and stress concentrations [23]. Nonetheless, a small number of studies have considered stress states other than uniaxial in AM materials [6,24,25].

In each of Sections 3–5, following the findings in Part I, effect of build orientation, process parameters and fabrication machine, heat treatment, and surface condition are evaluated, where possible. Subsequently, the failure mechanisms of the specimens with different conditions is discussed in these sections and compared across heat treatments and surface conditions.

Since the source of fatigue damage initiation in AM metals is often internal and surface defects, it is alluring to attempt to predict the fatigue life from the characteristics of observed defects. It is generally believed that fatigue strength of a component is governed by its largest defects [26]. The concept of Extreme Value Statistics (EVS) along with Murakami's area parameter which was described in Part I [1] has recently been adopted in several studies to estimate the largest expected defect in AM materials for use in fatigue life predictions and has shown to provide promising results [8,27]. The utilization of these methods to predict fatigue life based on internal and surface defects is discussed in Section 6.

Mechanical properties collected from small laboratory specimens might not fully represent the actual behavior of a part made of the same material [28,29]. This discrepancy arises from factors that are not typically probed in a coupon scale test. These include stress concentration and gradient effects, size/scaling effects, joint and contact stresses, residual stresses, environmental effects, and load history effects. These issues are discussed in Section 7.

2. Fabrication processes, specimen geometries, and heat treatments

Two LB-PBF machines were used to fabricate the specimens in accordance with ASTM Standard B348 [30]. These are referred to as M290 and AM250 throughout the paper. M290 used a laser power of 285 W, scanning speed of 1200 mm/s, hatch distance of 140 μm, and layer thickness of 30 μm. AM250 used a laser power of 400 W, scanning speed of 1000 mm/s, hatch distance of 160 μm, and layer thickness of 50 μm. Both machines used an Argon shielding gas during fabrication. For more information about the fabrication details the reader is referred to [6,24].

Two different specimen geometries were utilized to perform the fatigue tests. Round solid specimens were used for axial fatigue tests and thin-walled tubular specimens were used for some axial, but mostly torsion and multiaxial fatigue tests. Thin-walled tubular specimens were designed in accordance to ASTM Standard E2207 [31] maintaining the thin-wall assumption. These specimens were used for torsion and multiaxial fatigue tests in order to minimize shear stress gradient in torsion. For more information about the round solid and thin-walled tubular specimen geometries, the reader is referred to [32] and [6,24], respectively. All of the data in this paper are for these specimen geometries, unless otherwise specified.

Common heat treatment processes for AM Ti-6Al-4V alloy were discussed in Part I, with three common cases considered here: (1) non-heat treated (n-HT) condition which consisted of specimens subjected to no subsequent heat treatment processes, (2) below the β-transus temperature annealed/stress relieved condition which consisted of preheating the furnace to 700 °C and leaving the samples inside the chamber for 1 h with supplying Argon gas followed by free convection air-cooling at room temperature, and (3) Hot Isostatic Pressing (HIP) which consisted of 920 °C and 100 MPa for 3 h in accordance to ASTM Standard F2924 [33]. HIP is an effective thermo-mechanical treatment that acts to reduce the volume of internal defects such as Lack of Fusion (LOF) defects, which are known as a major detriment to fatigue performance of AM parts. The microstructural specifications of the as-built, annealed, and HIPed specimens were presented in Part I [1].

3. Axial fatigue behavior

3.1. Effect of defects

In High Cycle Fatigue (HCF) or Very High Cycle Fatigue (VHCF), the majority of the fatigue life is spent in the initiation and early propagation of embryonic fatigue cracks [34–36]. In general, fatigue cracks typically initiate by plastic slip which is governed by the local microstructure. In wrought polycrystalline alloys, saturation of fatigue stress is associated with the formation of localized well-regulated dislocation substructures, such as persistent slip bands in most Face Centered Cubic (FCC) and some Hexagonal Close Packed (HCP) metals [37], or dislocation cells in Body Center Cubic (BCC) and most HCP metals. Such substructures localize the macroscopically-applied deformation into finite slip bands, which carry large amounts of shear deformation [38–40]. Fatigue cracks can then be formed at the free surface or along grain boundaries by the intrusion-extrusion mechanism [41–43]. As such, microstructure attributes are key to fatigue performance.

For AM metals, in HCF and VHCF regimes, stress concentrations at and near defects can facilitate localized plastic deformation, even though the macroscopic mechanical response appears to be elastic [44,45]. In traditional alloys, localized plastic deformation leads to the formation of low energy sub-grain dislocation structures at saturation, whose irreversible plastic deformation leads to cyclic damage and ultimately fatigue crack initiation [46–49]. The extent of the plastic deformation surrounding defects depends on multiple factors including the shape, size and location (e.g. nearest neighbor defect, or distance to the free surface) of the defect and the characteristics of the surrounding microstructure (i.e. phase composition, crystal orientation, and grain size). From the perspective of linear elastic fracture mechanics, the size and shape of the defect are key in the earliest stages of crack growth, with large LOF defects being most detrimental to fatigue performance.

A subset of literature data was examined to demonstrate how α-colonies/prior-β grains, LOF defects or spherical pores can impact the HCF strength of AM Ti-6Al-4V focusing on manuscripts where both fatigue life and Crack Initiation Site (CIS) fractography were reported for both powder feed AM (laser and electron beam) and traditionally fabricated wrought materials [11,12,14,15,17–20,50–59]. In Fig. 2, the HCF strength is defined as the effective stress of a fatigue cycle that corresponds to a fatigue life of 10^6 cycles, interpolated from the reported S-N (i.e. stress-life) curves. To compensate for variation in stress ratio (R) across the data, the concept of an effective stress was used, following Eq. (1) [60]:

$$\sigma_{\text{eff}} = \sigma_{\max}\left(\frac{1-R}{2}\right)^{0.28} \tag{1}$$

The CIS was estimated from the root of the projected area of the defect in the direction of loading. Given that samples do not fail at exactly 10^6 cycles, inference was required using nearby data points.

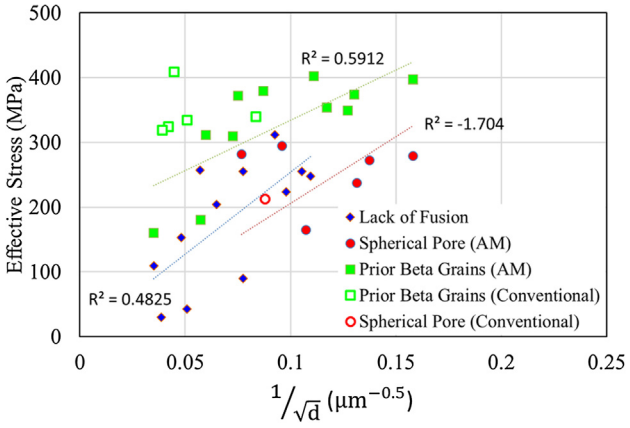

Fig. 2. Correlation between effective stress and crack initiation site (CIS) size for different CIS types: LOFs, spherical pores, and α-colonies/prior-β grains. Hollow data points corresponding to wrought samples.

Additionally, the typical CIS size was obtained from the reported defect sizes of the corresponding sample batch. When multiple CISs (namely, LOF, spherical pores, or α-colonies/prior-β grains) were reported, then the CIS with the highest expected stress intensity was used, noting that LOF defects have significantly higher stress intensity factors than spherical pores. If crack initiation was not associated with a defect, it was assumed to be due to the localization of slip, as occurs in wrought material and measured from the initial crack zone (flat area at the CIS). This type of failure has been reported in HIPed AM Ti-6Al-4V samples [54], where the propensity for cracks to initiate from defects has been decreased. Samples with bi-modal microstructure, horizontally-built and 45°-built samples were excluded from the dataset.

It is apparent from Fig. 2 that the HCF strength is generally (but not always) the greatest when the CIS does not correspond to a LOF defect or spherical pore. The difference in HCF strength between the LOF defect and spherical pore CISs is not discernible among the data shown. Further, the HCF strength is not strongly correlated with size for any of the CIS types, which is consistent with AM literature, for example [61]. While these two points contradict the often-used linear elastic fracture mechanics vantage, this is not necessarily surprising considering the length scales involved, e.g. plastic zone size vs CIS size, and potential for strong nonlocal effects, e.g. grain characteristics within the neighborhood of the CIS. In support of this point, it is worthwhile to note that in some cases the HCF strength of wrought or HIPed AM Ti-6Al-4V samples was inferior to non HIPed AM samples with LOF-type CISs.

3.2. Effect of build orientation

As discussed in Part I [1], various design and processing parameters such as shape and size of the part as well as its build orientation can influence the microstructure and defect characteristics. Specifically, directional prior-β grain growth along the build direction can result in microstructural anisotropy in the part and hence anisotropy in many aspects of the mechanical performance. For instance, Carroll et al. [62] reported significant anisotropy in the ductility of laser-based DED Ti-6Al-4V related to the grain boundary α-phase, along the prior-β phase boundaries, being subjected to tensile opening modes for loading directions perpendicular to the build direction. In fact, anisotropy in the Low Cycle Fatigue (LCF) behavior has been reported and attributed to the anisotropy in ductility related to the directional prior-β microstructure [63]. Though it has been shown that process conditions governing the cooling rate during solidification can affect the presence of the columnar prior-β microstructure [64], the relationship between build orientation, microstructure, process induced defects, and the resulting fatigue performance requires attention.

As discussed in [28,65], the aspect ratio and build orientation can influence the thermal history and, therefore, the residual stresses, resultant microstructure, and the orientation and shape of the defects. For non-heat treated and annealed conditions in the literature, for example in [10,51,66,67], build orientation anisotropy of fatigue performance has been reported. Generally, vertically fabricated samples are found to have shorter uniaxial fatigue lives than samples fabricated in other directions. This is often attributed to the projected area of the LOF defects normal to the loading axis being larger for the vertically built samples. For instance, some strong anisotropy in the fatigue behavior of other AM materials, 17-4 PH and 316L stainless steels, has been recently reported by the co-authors [28,68,69]. Horizontally fabricated samples were found to have longer fatigue lives than samples fabricated in vertical orientation. The authors concluded that the anisotropy observed in the fatigue behavior of these materials is due to the fact that the projected area of the LOF voids on the loading plane are different for vertically and horizontally fabricated specimens.

Edwards and Ramulu [51] reported significant anisotropy for LB-PBF Ti-6Al-4V related to build orientation of the specimens with fractography images suggesting the presence of LOF defects at the CIS. In another recent study, LB-PBF Ti-6Al-4V specimens were fabricated in vertical, diagonal, and horizontal directions [32]. The presence of pores was reported for all build orientations, however, fractography analysis revealed the pores at the crack initiation sites to be spherical rather than slit shaped LOF defects. The projected area of these spherical pores on the loading plane is almost the same regardless of build orientation; therefore, little anisotropy was observed between the different specimen orientations. Fig. 3(a) and (b) show similar performance of annealed Ti-6Al-4V coupons for three build orientations and two surface conditions [32,70]. Further, specimens subjected to HIP processing, often show little or no anisotropy in fatigue performance [6,7,71], where LOF defects and spherical porosity are often minimized. The

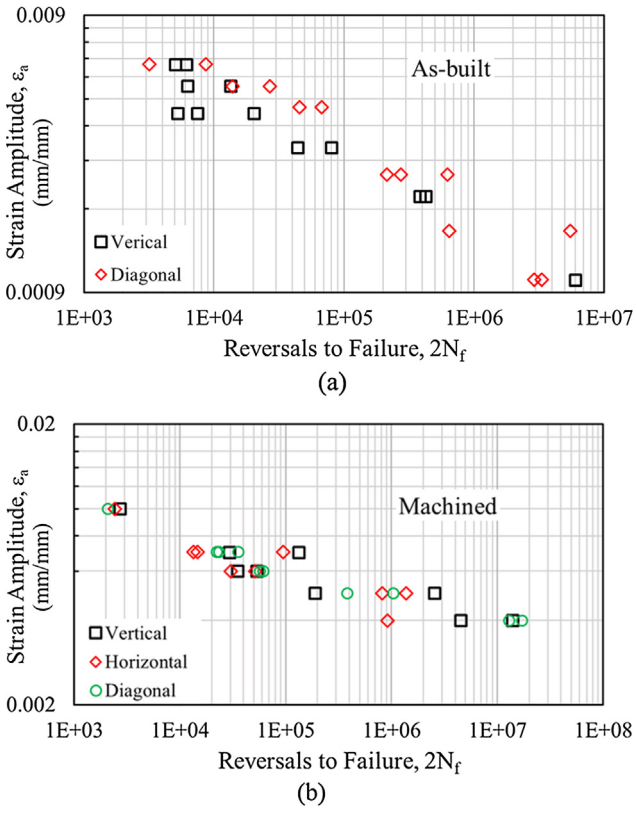

Fig. 3. Superimposed results of fully-reversed axial fatigue tests for LB-PBF annealed rod specimens with different build orientations for (a) as-built surface, and (b) machined surface conditions [32,70]. The specimens are fabricated with M290 machine.

findings suggest that, despite the directional prior-β grain structure of LB-PBF Ti-6Al-4V, anisotropy in the HCF behavior is mostly a function of the character and presence of LOF defects influencing fatigue crack initiation and propagation rather than microstructural characteristics.

3.3. Effect of residual stresses

As discussed in Part I [1], residual stresses can be removed or at least minimized during or after the fabrication process. The fabrication process parameters, build orientation, and post fabrication heat treatment can all play a role in the resulting residual stress. If significant residual stresses remain, they can act as an additional fatigue crack driving force and need to be considered in fatigue life analysis.

Several studies in the literature confirm the effect of different post fabrication heat treatments in eliminating or reducing residual stresses. For example, Leuders et al. [72] measured the residual stresses in LB-PBF Ti-6Al-4V specimens and observed that the stress relieving heat treatment at 800 °C for 2 h reduced the as-fabricated 200 MPa residual stresses to less than 5 MPa after the treatment. It was observed that this process improved the fatigue life by about a factor of four at the mid-life regime. They also found that the stress relieving treatments resulted in a fatigue crack growth behavior similar to the wrought Ti-6Al-4V material. Vrancken et al. [73] also observed that residual stresses have a significant influence on the anisotropic crack growth behavior of the compact tension specimens of LB-PBF Ti-6Al-4V fabricated in different orientations. In another study, Benedetti et al. [74] measured the residual stresses in LB-PBF Ti-6Al-4V specimens with different conditions and observed that HIPing the samples at 920 °C and 100 MPa for 2 h could completely remove the residual stresses. The time required to relax the residual stress in LB-PBF Ti-6Al-4V can be estimated by a simple visco-plastic material model with parameters chosen to match the high temperature material behavior [61]. For example, it takes ~ 10 mins for residual stresses to decrease from yield (951 MPa) to 5 MPa at 800 °C [61].

It has been shown that the scanning strategy can also have significant effects on residual stresses and, subsequently, on the mechanical properties of the fabricated parts [75,76]. For instance, Ali et al. [75] examined different scanning strategies on LB-PBF specimens including 45° alternating, 90° alternating, and several chessboard strategies with different sizes and different scan vectors in adjacent blocks. They found that different strategies result in different residual stresses. In another study, Casavola et al. [77] showed that the magnitude of residual stress is affected by the part thickness and position of the fabricated LB-PBF parts in the chamber. The challenge in relating residual stress effects to processing and post processing parameters is that the parameters are also related to the defect characteristics, which can also govern fatigue performance. To date, we are not aware of efforts that have sought to isolate coupled effects, beyond standard stress-relieving heat treatments at low temperatures which are intended to have a mild effect on the microstructure.

3.4. Effect of post fabrication heat treatments/HIP

As discussed extensively in Part I [1], different heat treatments could transform the less ductile martensite microstructure of fabricated AM Ti-6Al-4V parts to a more ductile equilibrium $\alpha + \beta$ phase and also change the amount of residual stresses. Therefore, the failure mechanism of the material under different heat treatment conditions may differ due to differences in the microstructure and defect characteristics of the material. For additive manufactured Ti-6Al-4V material, the low ductility in conjunction with the presence of defects often results in poor fatigue performance, and subsequent heat treatments to regulate the part microstructure/ductility can be advantageous [51]. However, the ductility of HT samples can still be noticeably lower than that of conventional wrought specimens.

The improvement in ductility of AM Ti-6Al-4V parts through HT has been mostly inconsistent with varying degrees of success being reported in the literature [78–82]. Obtaining a coarser α microstructure can also lead to additional improvements in ductility in which the α width is mainly determined by the maximum soak temperature followed by holding time. The best performance is often found at temperatures just below the β-transus temperature, however, the columnar prior-β microstructure is preserved, which was shown to contribute to anisotropy in the LCF regime. Many researchers have shown significant improvements in ductility such that the elongation to failure required by ASTM F1472 and F2924 [33,83] are obtained for LB-PBF Ti-6Al-4V.

Leuders et al. [72] showed that heat treatments consisting of soak temperatures of 800 °C and 1050 °C resulted in subsequent improvements in ductility from 1.6% for the as-fabricated material to 5% and 11.6% respectively. This improvement in ductility coincided with an increase in HCF performance. The mean fatigue lives for as-fabricated specimens was approximately 29,000 cycles while the 800 °C HT specimens resulted in an improvement to 93,000 cycles and the 1050 °C HT specimens improving to 290,000 cycles. While significant improvements in HCF performance was observed for the heat-treated specimens, the performance was still lower than what is typically observed for conventional Ti-6Al-4V.

Leuders et al. [72] also showed that HIP treatment was successful in improving the ductility, in addition to reducing the size of the porosity, resulting in a fatigue limit comparable to conventional wrought Ti-6Al-4V. In fact, AM Ti-6Al-4V parts post processed with HIP and a subsequent surface machining have been well established to have fatigue performance on par with traditional wrought Ti-6Al-4V [6,61]. Fig. 4 shows the superimposed axial fatigue test data of the wrought and HIPed LB-PBF machined surface Ti-6Al-4V tubular specimens with different build orientations [6]. As can been seen, the fatigue performance of HIPed LB-PBF specimens is not only comparable with the wrought material, but also shows no substantial difference between different build orientations (vertical versus diagonal (45° built) specimens). As discussed in [61], the effectiveness of HIP treatment in improving the fatigue performance of AM material, relative to other heat treatments, can be attributed to a combination of decreasing crack initiating defect sizes below a threshold and changing the microstructure around the defects. This finding was supported by a quantitative Electron Backscatter Diffraction (EBSD) observation of a more refined microstructure surrounding the defects in HIPed LB-PBF Ti-6Al-4V [61].

Due to the presence of inherent build defects in AM parts, HIP treatment still seems to be a necessary post treatment procedure to obtain good fatigue performance. The behavior of the HIPed LB-PBF material was found to be ductile, and the failure mechanism to be shear. Failure orientation of HIPed samples under axial loading was along maximum shear planes [6]. The ductile behavior observed for HIPed specimens is also consistent with the findings of the monotonic test results in [6]. The combined effects of microstructural transformation to a more ductile $\alpha - \beta$ phase, and removal or significant shrinkage of

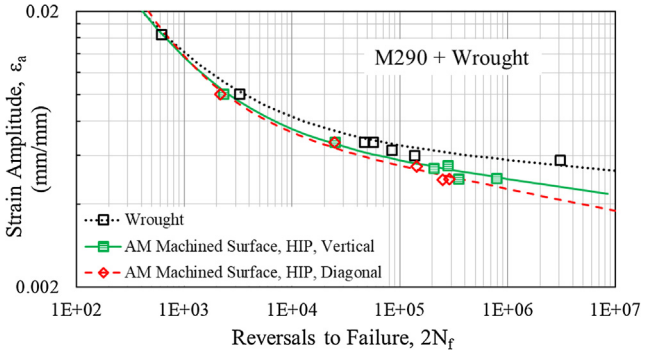

Fig. 4. Superimposed results of fully-reversed axial fatigue tests for wrought and LB-PBF HIPed machined surface tubular specimens with different build orientations fabricated with M290 machine [6].

the internal defects are the main contributors for this behavior [6].

3.5. Effect of surface roughness

Although the capability to fabricate complex and/or near net shape geometries is one of the most promising advantages of AM, relative to conventional manufacturing techniques, it is currently not achievable for fatigue critical AM Ti-6Al-4V builds due to the requirement for post-build surface treating. Topographic surface features can function as initiation sites for fatigue cracks and thus can play a substantial role in determining fatigue life. As discussed in Part I [1], the surface topography of AM builds is tortuous due to the partially melted powder particles, and in the cases of curved surfaces the discrete layer-wise building process. Therefore, the effects of surface finish on the fatigue behavior is an important consideration in fatigue analyses and design of AM parts.

AM Ti-6Al-4V specimens tested in the as-built surface condition resulted in fatigue lives up to four times shorter than their machined and polished counterparts in [84,85]. It is generally understood that the rough surface of as-built specimens creates stress concentrators that lead to earlier crack initiation. Fig. 5 provides a comparison of strain-life fatigue data for both as-built surface and machined surface specimens fabricated in vertical and diagonal (45° to the build plate) directions [70]. Regardless of the build direction, the fatigue resistance of specimens with rough as-built surfaces is much lower than the machined surface specimens, especially in the HCF regime. At the strain amplitude of 0.004 mm/mm, the as-built surface condition results in a fatigue life a few orders of magnitude shorter than the specimens with machined surfaces.

As it was discussed in Part I [1], surface roughness can be affected by both process conditions and post-process surface treatments. Previous work on the fatigue behavior of Ti-6Al-4V produced by LB-PBF revealed that increasing mean roughness, R_a, correlated with decreasing fatigue resistance [65]. Fractography analysis showed that, in the presence of high surface roughness, cracks initiate at many locations throughout the uniform gage section. The deep valleys of the surface roughness act as micro-notches resulting in micro-cracks initiating from the specimen surface. These cracks grow independently until they become large enough to interact and coalesce into a single large dominant crack, after which failure occurs abruptly. This crack initiation and growth behavior is much different as compared to machined surface specimens where cracks typically initiate at a single defect and grow until failure with little to no evidence of crack coalescence on the fracture surface [65]. This interaction between several cracks can compound the effects of early life crack initiation induced by surface roughness and further contribute to the detrimental effect on the HCF performance of AM Ti-6Al-4V.

Chan et al. [84] compared the effect of surface roughness on the mean fatigue lives of both E-Beam PBF and LB-PBF Ti-6Al-4V specimens at a stress range of 600 MPa with stress ratio of 0.1. The E-Beam PBF specimens had much higher surface roughness and much lower fatigue strength compared to the LB-PBF specimens. Greitemeir et al. [86] also compared the fatigue behavior of both LB-PBF and E-Beam PBF fabricated Ti-6Al-4V and were able to make reasonable fatigue life predictions using a fracture mechanics based approach. This approach uses max peak-to-valley, R_t, as an equivalent initial flaw size. However, R_t may not be truly representative of the initial flaw size as the particles only partially fused to the surface would not be expected to contribute greatly to the stress concentration induced by the rough surface. Instead, the deepest valleys of the surface roughness and the shape of these valleys would be expected to be the main source of stress concentration. The radius of curvature at the valleys protruding into the part, along with other surface roughness parameters, may give better approximations of the surface roughness effects by also considering the shape of the micro-notches.

Pegues et al. [87] also tried to predict fatigue life of LB-PBF Ti-6Al-4V as-build surface specimens by considering several roughness parameters such as max peak-to-valley (R_t), 10-point height (R_{zISO}), and the 10-point valley radius ($\bar{\rho}$) for three different specimen types with varying surface roughness. These roughness parameters and material ultimate tensile strength were used to approximate the effective elastic stress concentration factor, K_t, which was then employed to estimate the fatigue notch factor, K_f. These factors were then used to predict the stress-life fatigue curves which showed acceptable correlations to experimental fatigue data. Though the curves were slightly non-conservative, the approach provided reasonable estimations without the need for excessive fatigue testing.

4. Torsion fatigue behavior

Unlike the relatively large number of uniaxial fatigue test data for AM metallic materials discussed in the previous section, there is limited fatigue test data on these materials under other loading conditions such as torsion fatigue loading [24,88]. An important challenge associated with torsion loading is the shear stress gradient through the cross section, making it difficult to compare with fatigue behavior under uniform stress states, such as in uniaxial loading. This could be more critical for AM parts, where internal defects are inevitable part of the manufacturing process and they are non-uniformly distributed. Defects closer to the outer surface will also have more detrimental effect under torsion loading which is associated with higher stress resulting from the shear stress gradient.

4.1. Effect of build orientation

It is generally believed that the detrimental effect of defects on the fabricated part's fatigue strength can vary with defect-loading

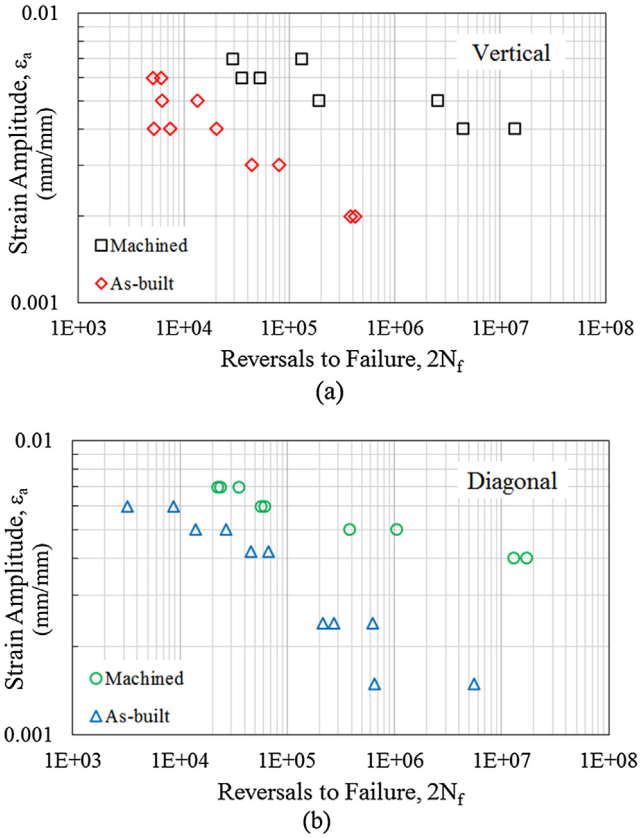

Fig. 5. Fully-reversed strain-life fatigue behavior for machined surface and as-built surface LB-PBF specimens built in (a) vertical and (b) diagonal orientation [70].

alignment, where the fatigue strength could substantially improve if the loading direction is parallel to the common alignment of defects [29,68]. This, however, becomes more complex under torsion loading due to the fact that the failure orientation is not necessarily perpendicular to or aligned with the loading direction. As an example, failure orientations of ductile and brittle behaving materials under torsion loading are shown in Fig. 6 for vertical and diagonal built (at 45°) specimens. As can be seen, cracks could align at different orientations based on the build orientation as well as the failure mode of the material.

Improving the fatigue performance of the AM materials under different loading conditions may be possible by considering the applied stress state and the expected failure mechanism. The fatigue life of AM parts could be improved by developing the directionally fabricated materials in which the best performance direction is aligned with the most critically loaded plane orientation [28].

Build orientation effect under torsion loading was studied by Molaei et al. [6] on LB-PBF HIPed specimens of Ti-6Al-4V fabricated in vertical and diagonal (at 45°) orientations. Similar to the findings in the literature for uniaxial loading, generally no anisotropy effect in fatigue performance was observed for HIPed samples built in different orientations, as shown in Fig. 7. Neutralizing the fatigue crack initiating defects, resulted in reduction of the anisotropy of the samples. This is in addition to HIP's homogenization effects on the microstructure resulting from recrystallization of the alpha phase.

However, it was discussed in [6] that diagonal specimens show somewhat longer fatigue lives under torsion loading, while shorter lives were achieved under axial loading conditions as compared to the vertical specimens. This was contributed, in some degree, to the orientation of LOF defects which are roughly oriented perpendicular to the build direction [6]. Defects in the vertical specimens are along one of the maximum shear planes under torsion loading, while they are along one of the maximum shear planes for the diagonally built specimens under axial loading, as can be seen from Fig. 6 for torsion loading, knowing that LOF defects are perpendicular to the build direction. Therefore, as the expected failure plane and build direction become closer to being perpendicular, probability of failure increases.

4.2. Effect of fabrication machine and processing parameters

As presented in Part I [1], variations in process and design parameters can significantly affect the microstructure and defect characteristics. In order to better understand this variability, both monotonic tensile and torsion fatigue test results of LB-PBF Ti-6Al-4V samples fabricated by the two LB-PBF machines (referred to as M290 and AM250 in Section 2) were compared to each other in [6]. As mentioned earlier, the two machines used different processing parameters to fabricate the specimens.

The fatigue performance of the fabricated specimens with aforementioned fabrication machines support the assertions made earlier in Figs. 1 and 2. Fig. 8 shows significantly different fatigue performance between the vertical as-built surface HIPed specimens fabricated with these machines. This is because the size and density of defects in the two specimen sets were very different. Further, considering that the monotonic stress versus strain curves were nearly the same [6], the point of Fig. 1 is also reinforced, i.e. the ultimate strength does not correlate with fatigue performance, and is not a reliable indicator of the cyclic response of the material.

4.3. Effect of post fabrication heat treatments

Selecting appropriate processing parameters and build orientations could decrease the residual stresses that result from the fabrication process. It was discussed in Part I [1] that the remaining residual stresses could be removed with proper post fabrication heat treatment processes. Moreover, it was discussed that if these post fabrication heat treatments are applied at proper temperature and duration, they could significantly improve the ductility and, therefore, would likely reduce the notch sensitivity of the materials to defects. In addition to the regular heat treatment and annealing processes, HIPing as a thermo-mechanical treatment can neutralize defects.

Fig. 9 shows the effect of different heat treatment processes on torsion fatigue behavior of the as-built surface and machined surface specimens [6,24]. By comparing the torsion fatigue test results with and without annealing for both as-built surface and machined surface specimens in Fig. 9(a), improvements offered by the annealing process become evident. As can be seen in this figure, regardless of the surface condition, annealing improved the fatigue behavior of the specimens by more than an order of magnitude. Although no significant change in ductility or microstructure was observed after the annealing process for the specimens in [24], the improvement was attributed to the relief of the residual stresses which were generated during the fabrication process.

No significant difference in fatigue life of the annealed and HIPed specimens in presence of the as-built surface condition is observed in Fig. 9(a). This highlights the importance of the subsequent surface finish step in the HIP process, given that the pressure associated with HIP treatment does not act on defects that are connected to the surface. Therefore, when considering the HIPing process, removal of a certain amount of material from the surface, depending on the distribution of the surface defects is necessary in order to see significant improvements in the fatigue performance of HIPed samples. This can be seen in Fig. 9(b) for machined surface annealed and HIPed vertical and 45° specimens, where HIPed specimens exhibit longer lives as compared to the annealed specimens. In addition, no substantial difference can be observed between the fatigue performance of the machined surface specimens built in different orientations after performing the HIP process. However, capability of post fabrication heat treatments including HIP in eliminating the anisotropy of the AM fabricated parts could still depend on several factors including fabrication process parameters and their induced defects with respect to size, density, surrounding microstructure, as well as residual stresses [89].

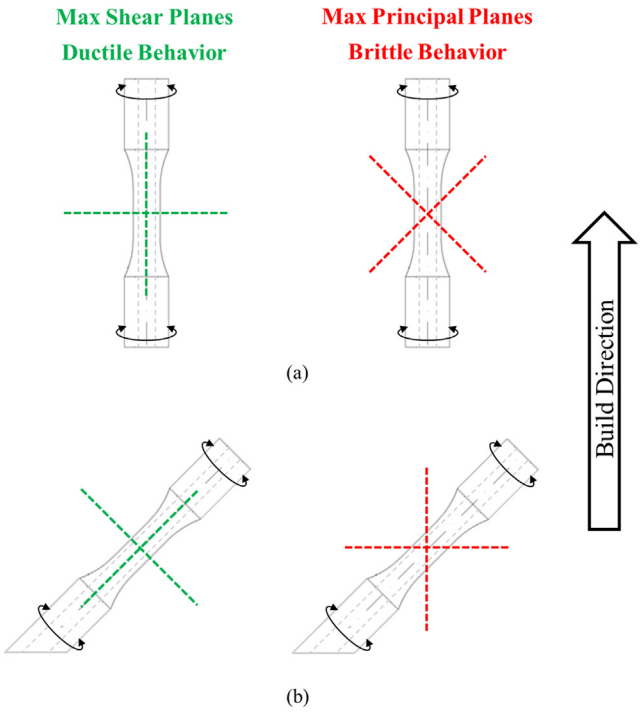

Fig. 6. Schematic view of predicted failure crack orientations for ductile and brittle behaving materials under torsion loading (a) vertical built, and (b) 45° built samples.

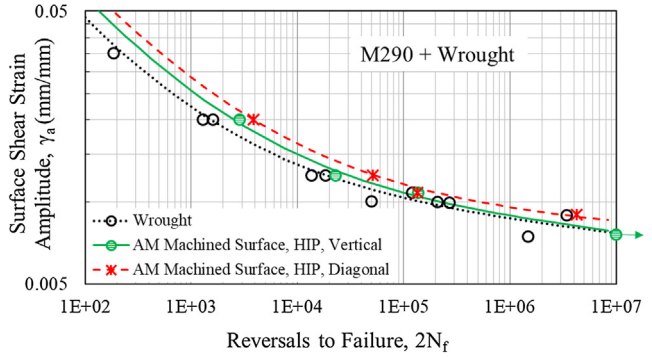

Fig. 7. Superimposed results of fully-reversed torsion fatigue tests for wrought and LB-PBF HIPed machined surface tubular specimens with different build orientations [6].

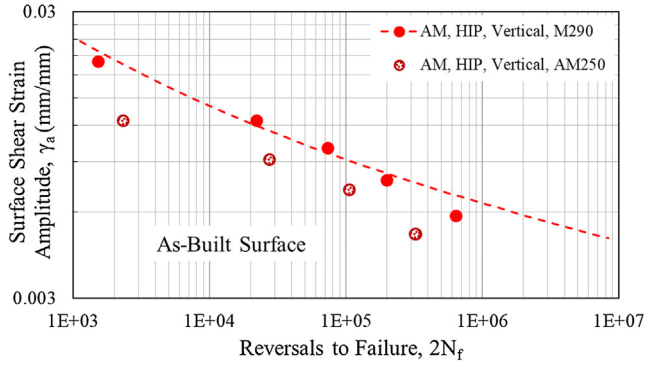

Fig. 8. Effect of fabrication machine and processing parameters on torsion fatigue behavior of LB-PBF as-built surface HIPed Ti-6Al-4V alloy [6].

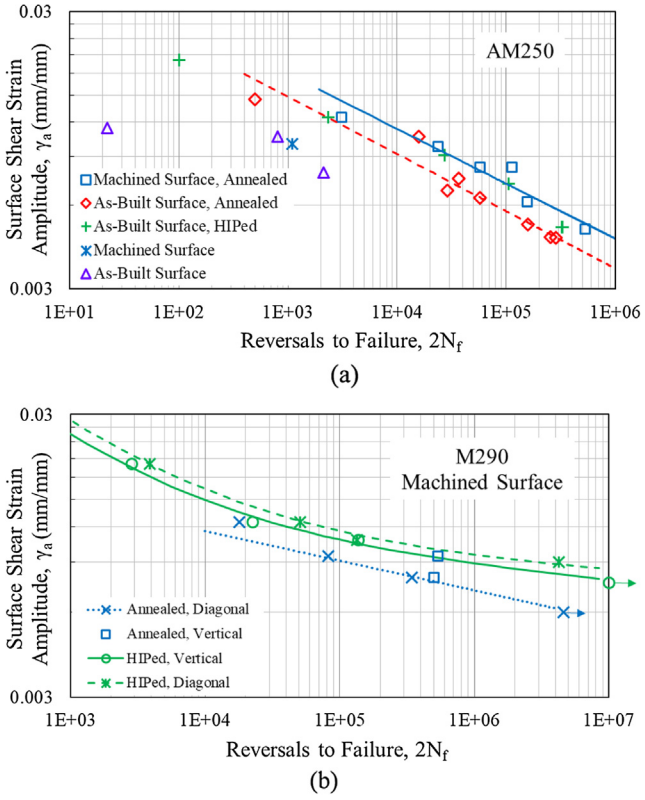

Fig. 9. Effect of heat treatment on fully-reversed torsion fatigue tests: (a) as-built, annealed, and HIPed specimens with different surface conditions fabricated with AM250, and (b) annealed and HIPed machined surface specimens fabricated with M290 [6,24].

4.4. Effect of surface roughness

Fig. 10(a) compares the LB-PBF as-built surface and machined surface torsion fatigue test results for the annealed condition reported in [24]. The wrought curve in this figure is shown as a reference from the same study for comparison to the AM specimens. It can be seen from this figure that the surface machining results in consistently longer fatigue lives by an average factor of about 4. This agrees well with the data presented in Fig. 5 for uniaxial loading. Surface machining removes the stress concentrations associated with the rough surface and the material that was deposited near the surface. The improvement is not as significant as that expected for conventional wrought metallic materials, due to the existence of interior impurities/defects which are not affected by the surface treatment and result in detrimental effects on the fatigue performance. This effect is similar to that in castings which contain porosity and/or other defects.

Comparison of as-built surface and machined surface test results of HIPed Ti-6Al-4V specimens is shown in Fig. 10(b). As can be seen in this figure, the fatigue performance of the machined surface samples is improved, as compared to those with the as-built surface condition. This difference becomes more pronounced at longer lives, again indicating a more substantial effect of defects in controlling the fatigue behavior in HCF. Comparison between this figure and Fig. 9(a) indicates that the best fatigue performance is observed only after machining the HIPed samples. Masuo et al. [90] observed a similar behavior regarding to the importance of the surface finish after performing the HIP process under axial loading.

4.5. Failure mechanism

The failure mechanisms and cracking behaviors were identical for machined surface specimens fabricated with two different machines and process parameters. Shear failure (failure along the maximum shear planes) was observed at higher shear stress levels for both specimen sets, while tensile failure (failure along the maximum principal planes) was observed as the stress level dropped. In addition, there was no difference between the cracking behavior of the vertical and diagonal specimens [6]. This is in spite of the microstructure, ductility, and defect characteristics differences for M290 and AM250 fabricated samples in annealed condition due to different fabrication parameters. However, due to the aforementioned differences, fatigue life of the fabricated specimens with these two machines were very different. For example, a M290 fabricated specimen under shear stress of 348 MPa failed after about 250,000 cycles, while the specimen fabricated with AM250 failed after only about 29,000 cycles under the same shear stress.

A dependence of crack growth direction on loading level was also observed for both annealed and HIPed conditions. As the loading level increases, longer mode-II cracks grow on planes of maximum shear before branching to maximum tensile planes. Gates and Fatemi [91] showed that friction and roughness induces crack closure, caused by crack face interaction, play a key role in determining the crack path. They showed that at the lower loading levels, the combined effect of friction and roughness reduce the effective shear-mode driving force at the crack tip until it drops below a critical level. As the load level decreases, the crack initiates in mode-I direction, indicating the dominant influence of the internal defects at longer lives.

For machined surface HIPed specimens fabricated with M290, cracks were observed to initiate on or near the maximum shear planes, similar to the axial loading for the LB-PBF HIPed and the wrought material. This is attributed to the HIP process evolving the more brittle behaving α′ martensitic microstructure to a coarser, more ductile behaving α lamellar structure, in addition to the closure/shrinkage of the internal defects. Similar to the annealed condition, the crack growth

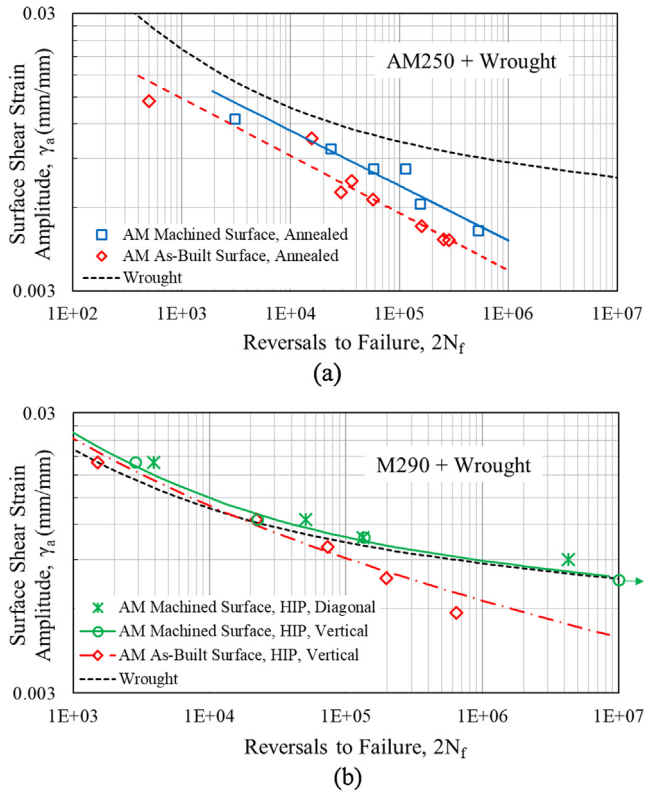

Fig. 10. Effect of surface finish on fully-reversed torsion fatigue tests and comparisons to the wrought data: (a) annealed specimens with as-built surface and machined surface conditions fabricated with AM250, and (b) HIPed specimens with as-built surface and machined surface conditions fabricated with M290 [6,24].

direction was dependent on the loading level. In addition, some other small cracks were evident at the vicinity of the failure crack. Shamsaei and Fatemi [92] showed that a larger number of micro-cracks initiate in more ductile behaving materials, as compared to the brittle behaving materials. Again, there was no substantial difference between the cracking behavior of the specimens fabricated in different orientation.

5. Multiaxial fatigue behavior

Multiaxial loads are very common for different components in many industries, and even under uniaxial or torsion loadings the stress state could be multiaxial due to the multidirectional residual stresses or complexities of the geometries with stress concentrations. Despite this fact, similar to the previous section for torsion fatigue study, only a few studies address the fatigue performance of AM Ti-6Al-4V alloy considering multiaxial loading conditions [6,25,93].

5.1. Multiaxial data under annealed condition

Combined in-phase and 90° out-of-phase axial-torsion test data of AM250 fabricated annealed specimens are shown in Fig. 11 for as-built surface and machined surface conditions based on von-Mises equivalent strain [25]. AM specimens have much shorter fatigue lives as compared to the wrought material, regardless of the surface condition and multiaxial load path applied. However, as can be seen in Fig. 11(a), surface machining improves the fatigue lives by a factor of about 4, which is due to the removal of defects concentrated close to the surfaces, similar to the observation for torsion loading discussed in the previous section. One factor in the lack of significant improvement in fatigue behavior of the machined surface AM specimens is the fine Widmanstätten microstructure that is present after annealing, as compared to the duplex microstructure of the wrought material. This is in addition to the existence of interior defects which become more detrimental by moving to the surface or near surface after the machining process. Hence, these defects act as the weakest-link for the material and cause crack initiations.

These findings are not surprising and consistent with uniaxial specimen test results from the literature. The inferior fatigue performance of the LB-PBF annealed axially loaded specimens in [25], regardless of the surface condition, as compared to the wrought condition, was attributed to the microstructure at shorter lives and the presence of internal defects such as LOFs and entrapped gas pores at longer lives. In some cases, LOF defects as large as 500 μm were observed for the fabricated specimens from AM250, resulting in significant shorter lives as compared to the reference wrought material.

5.2. Multiaxial data under HIPed condition

Fig. 12 shows the fatigue life of the in-phase and 90° out-of-phase axial-torsion tests of the machined surface LB-PBF HIPed M290 fabricated specimens in terms of von-Mises equivalent strain [6]. The wrought data are also included from [25] for comparison. Although most of the data are for vertically built specimens, a few test data are also included for 45° built specimens to show the HIPing effect on eliminating or reducing the anisotropy in multiaxial fatigue behavior. It is evident from Fig. 12(a) that there is no significant difference between the fatigue behaviors of vertical and diagonal (at 45°) specimens, after applying the HIP process. This is similar to the results of the axial and torsion fatigue tests discussed in the previous sections, where HIP significantly decreases the directionality of defects, as well as homogenizes the microstructure.

As can be seen from Fig. 12, there is no significant difference between the fatigue behavior of the machined surface HIPed AM and wrought materials. This indicates that if proper fabrication parameters

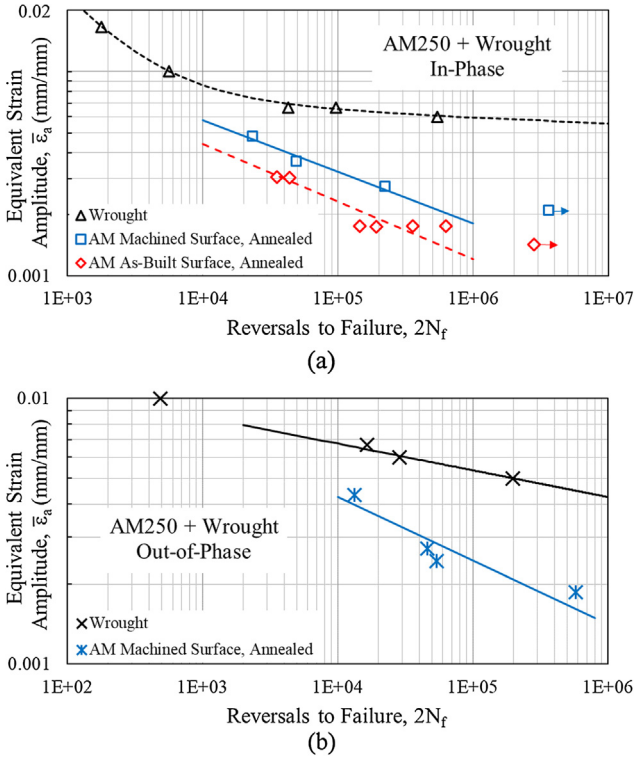

Fig. 11. Superimposed fully-reversed fatigue test results on wrought and AM250 fabricated annealed specimens under combined (a) in-phase, and (b) 90° out-phase axial-torsion loading conditions [25]. In part (b), the data point with plastic deformation is excluded from the fit.

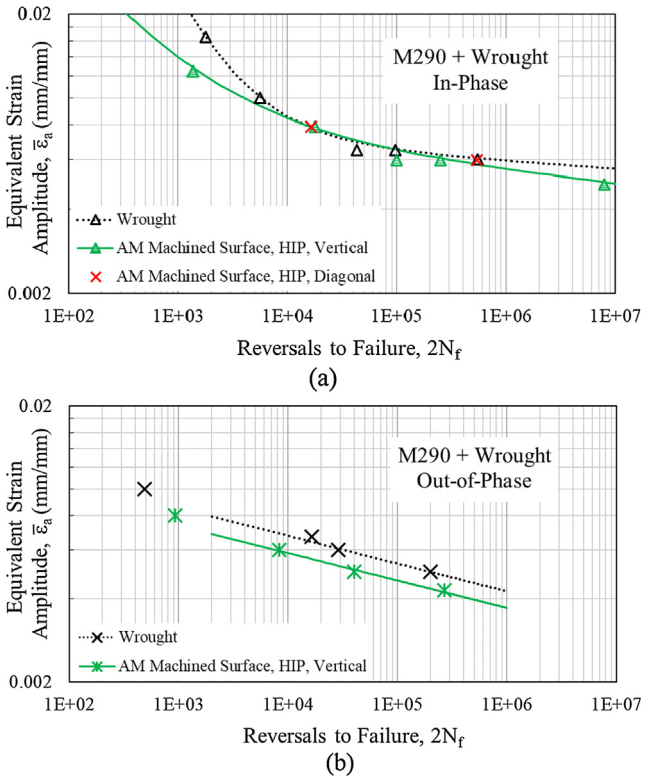

Fig. 12. Superimposed fully-reversed fatigue test results on wrought and machined surface HIPed specimens fabricated with M290 under combined (a) in-phase, and (b) 90° out-of-phase axial-torsion loading conditions [6]. LB-PBF specimens with different build orientations are included, when applicable. In part (b), the data points with plastic deformation are excluded from the fits.

are chosen for fabrication and, subsequently, appropriate post fabrication surface treatment and heat treatment processes such as HIP are applied to the material, it is possible to elevate the AM material fatigue performance to the level of the wrought material. The reasons for these improvements were already discussed in Sections 3 and 4 of this paper for axial and torsion fatigue behavior, as well as in Part I [1] of this two-part paper series.

Despite the similarity of the fatigue behavior of the AM machined surface HIPed material to the wrought material under different loading conditions (according to Fig. 4, Fig. 7, and Fig. 12), it was discussed in [6] that even after applying the HIP process, some interior defects as large as about 100 µm remained, which could act as CISs. Fig. 13 shows an example of a CIS caused by an entrapped gas pore under combined

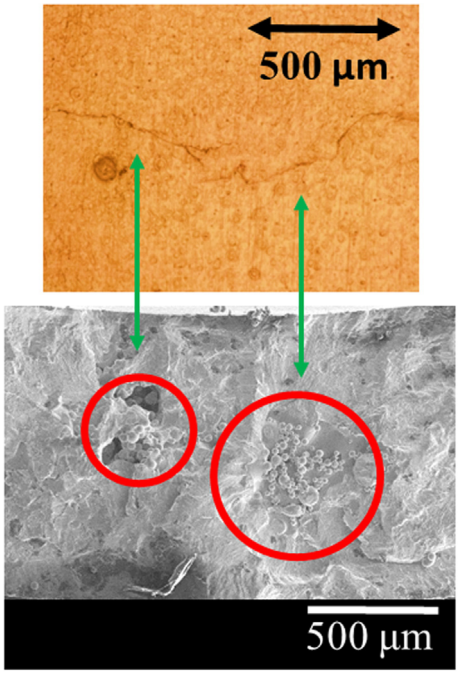

Fig. 14. Representative of internal cracks coalescence under combined in-phase axial-torsion loading on a machined surface annealed specimen fabricated with AM250 [94].

in-phase axial-torsion load. It was discussed in Ref. [6] that the microstructure of the AM material after HIP is much more uniform in terms of grain size and shape as compared to the less uniform equiaxed grains of the wrought material. In spite of the remaining defects in the AM HIPed condition, this is likely responsible for the similarity in the fatigue behavior of the wrought and the AM HIPed materials.

5.3. Failure mechanism

The failure mechanism under multiaxial loading can be influenced by the parameters of the post fabrication heat treatment, e.g. tensile failure was observed for the annealed condition and shear failure was observed for the HIPed specimens [6,25], similar to the axial and torsion loading conditions. For the HIPed specimens multiple small cracks were observed at the vicinity of the failure crack indicating a ductile behavior [92].

For some of the annealed specimen tests, crack orientation was observed to occur in an unexpected direction. Further investigation indicated that this could be due to the coalescence of several internal

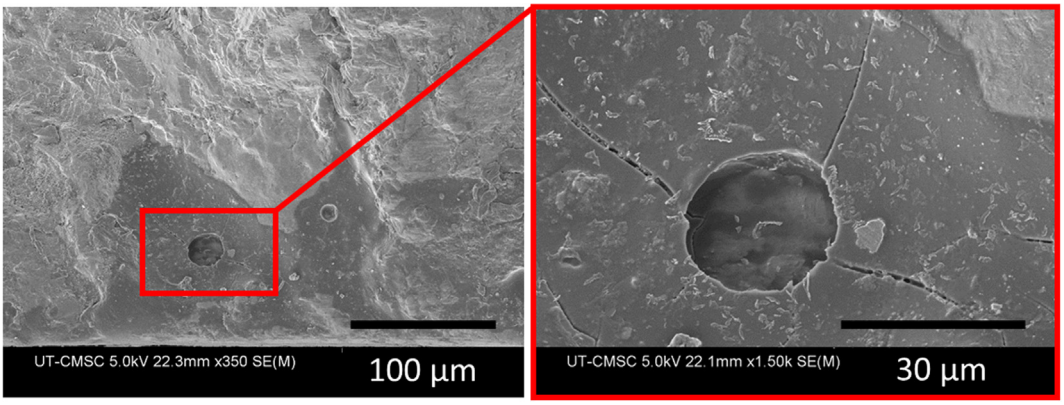

Fig. 13. Representative of fatigue crack initiation location of an LB-PBF machined surface HIPed specimen fabricated with M290 under combined in-phase axial-torsion loading. The failure is due to a relatively large porosity caused by entrapped gas [6].

defects. An example of this observation is shown in Fig. 14 for a combined in-phase axial-torsion test on an annealed specimen. As shown, two LOF defects grew individually up to the outer surface and joined together to form the failure crack. As can be seen, one of the cracks indicates mode-I orientation (i.e. tensile mode), while the other crack represents mode-II crack orientation (i.e. shear mode). Therefore, due to the presence of multiple internal defects in AM metals and their interaction during fatigue crack growth, it is possible to observe cracks with unexpected orientations [94].

5.4. Correlation of multiaxial fatigue data

Depending on the material microstructure and surface/sub-surface defects, fatigue behavior is mainly dominated by microcracks occurring near the maximum shear planes, along the maximum tensile plane, or other specific plane orientations due to different stress states. Therefore, appropriate damage models consistent with the damage mechanism and cracking orientation, often referred to as critical plane (s), are needed for correlating the multiaxial fatigue data.

Fatigue life correlations for all loading conditions of annealed specimens fabricated with AM250 are shown in Fig. 15(a) for the as-built surface and in Fig. 15(b) for machined surface condition based on maximum principal stress criterion. As can be seen, the data fall within the scatter band of ± 3× on life, regardless of the surface condition. This corresponds to and is consistent with the tensile failure mode of the annealed AM specimens observed in fatigue tests.

As discussed previously, the failure mechanism of the machined surface LB-PBF HIPed alloy was shear, therefore, a criterion which is appropriate for ductile behaving materials should be able to correlate the fatigue test results in this condition. It was observed in [6] that the commonly used von-Mises criterion failed to bring together fatigue data of the material, as can be observed from Fig. 16(a), while Fatemi-Socie critical plane parameter resulted in a reasonably good correlation of the data, shown in Fig. 16(b). This was attributed to the shear failure mechanism of the LB-PBF material in HIPed condition which was discussed earlier.

6. Modeling the effects of defects and surface roughness on fatigue life

As discussed earlier, the fatigue performance of AM metals is sensitive to the existence of defects. The aim of this section is to briefly discuss a method to predict the multiaxial fatigue life of AM metals based on some of the main defect characteristics discussed earlier. Prediction results are then compared with experimental results for validation of the model.

Murakami et al. [95] examined the correlation between the fatigue limit of clean steels and the CIS inclusion size defined by the square root of the projected area on the loading plane. This parameter has been implemented to represent defect size in several AM studies since the geometrical parameter √area reportedly allows calculating the maximum Stress Intensity Factor (SIF) along the front of an internal or surface crack with irregular shape [8,27]. The area of the defect is defined as an effective area of a smooth contour circumscribing the irregular defect shape. The rational for this definition is that the SIF on an irregularly shaped defect will drive the crack towards a round shape as it grows.

Murakami's approach relies on using EVS of observed/sampled defects to predict the size of the largest defect in a coupon, which is subsequently assumed to govern fatigue performance [96]. This approach has shown promising results for fatigue life prediction for uniaxial fatigue of AM material [27]. Given its popularity, an application of this approach is briefly examined here, by means of an effective defect size which is calculated for each loading case.

Fatigue life to crack initiation is defined here as a two-phase process. Phase-I is life to nucleate a crack from a defect and phase-II is the life associated with the growth of this small crack (typically up to less than 2 mm in length). This could be explained as the number of cycles to transform a "defect" to a "small crack" and then its propagation as a small crack to a size which corresponds to long fatigue crack growth behavior. For AM Ti-6Al-4V with crack initiating defects, it is common for the fatigue life to be considered as the growth life of a small crack [8]. Also, for the considered test specimens here, the fatigue life after reaching a crack length of about 2 mm is very short. The accuracy of life predictions based on this assumption depends significantly on the adopted small crack propagation model.

Various approaches to this small crack growth life could be adopted for correlation of the uniaxial and multiaxial fatigue life based on the material properties such as crack growth threshold, and cracking and failure mechanism of material. By closely observing material cracking and failure behavior, and analyzing fracture surfaces, the appropriate approach for fatigue life prediction for each material condition could be selected. The fatigue life prediction approach discussed here is based on a mode-I crack initiation and small crack growth from defects, for non HIPed LB-PBF Ti-6Al-4V specimens fabricated with AM250. Internal defect characteristics and surface roughness profiles of the corresponding specimens were analyzed, and the gathered information were further used for the fatigue life prediction based on defect and material characteristics.

Defect and roughness profile characterization and EVS calculations have been discussed in Part I [1] of this paper series. The experimental fatigue life data used in this study has been gathered from a previous study published by the authors on multiaxial fatigue performance of LB-PBF Ti-6Al-4V [25]. In this section, an effective defect size for the purpose of fatigue life modeling is presented, a generalized Paris equation is adopted for the material, and the prediction results are discussed for two cases of as-built surface and machined surface specimens.

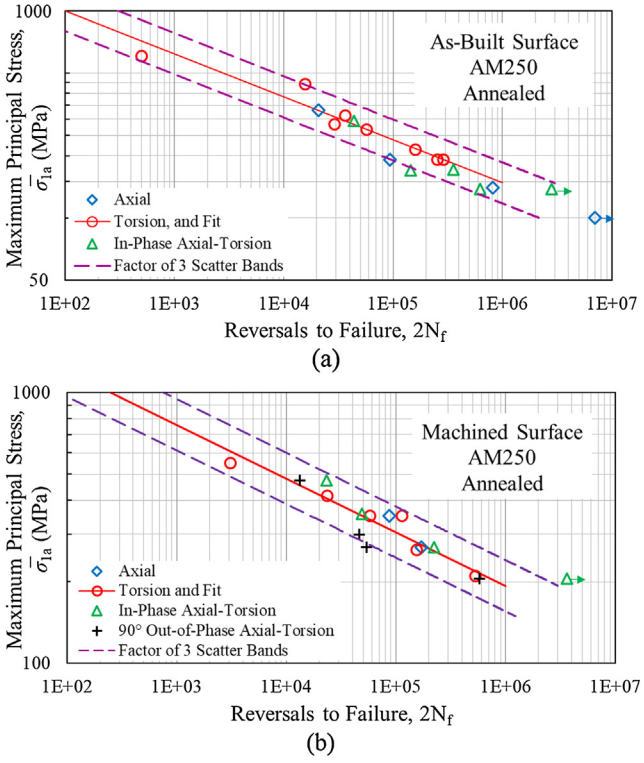

Fig. 15. Correlation of fatigue test results of LB-PBF Ti-6Al-4V alloy on: (a) as-built surface and (b) machined surface annealed specimens fabricated with AM250 based on maximum principal stress criterion [25].

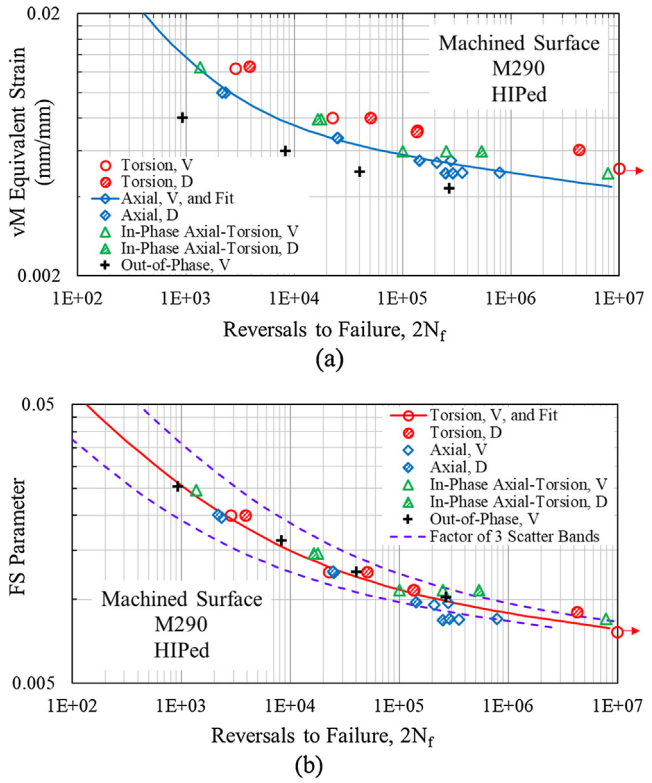

Fig. 16. Correlation of fatigue test results of LB-PBF Ti-6Al-4V alloy on machined surface HIPed specimens fabricated with M290 based on (a) von-Mises equivalent strain criterion and (b) Fatemi-Socie damage parameter [6].

6.1. Effective defect size

To incorporate the effect of defect size, an effective initial crack size represented as $\sqrt{area_{eff,max}}$ or the square root of the effective defect area can be defined based on the maximum prospective internal defect size ($\sqrt{area_{D,max}}$) and the maximum prospective equivalent surface defect size determined from the surface roughness profile ($\sqrt{area_{R,max}}$) as presented in Fig. 17 and applied to ductile cast iron [97]:

$$\sqrt{area_{eff,max}} = \sqrt{area_{D,max}} + \sqrt{area_{R,max}} \tag{2}$$

The equivalent surface defect size determined from the surface roughness profile $\sqrt{area_R}$ is calculated based on the work by Murakami et al. [98].

A stylus profilometer was used for measuring the surface roughness profile. To calculate the effective defect size based on the roughness profile and the method mentioned above, r is taken as the maximum predicted R_{max} from EVS (190.4 μm), t is the average pitch of the measured roughness profile (464.6 μm) as presented in Eqs. (3) and (4), and R_{max} is the largest of the successive values of $R_{t,i}$ calculated over the evaluation length of 17.5 mm ($i = 7$). The maximum prospective equivalent surface defect size ($\sqrt{area_{R,max}}$) was calculated by using EVS for the data gathered from the roughness profile of the specimens based on the method explained in the literature [97,98].

$$\frac{\sqrt{area_R}}{2t} \cong 2.97\left(\frac{r}{2t}\right) - 3.51\left(\frac{r}{2t}\right)^2 - 9.74\left(\frac{r}{2t}\right)^3 \quad r/2t < 0.195 \tag{3}$$

$$\frac{\sqrt{area_R}}{2t} \cong 0.38 \quad \frac{r}{2t} > 0.195 \tag{4}$$

The maximum prospective internal defect size ($\sqrt{area_{D,max}}$) for all AM250 annealed specimens and the maximum prospective equivalent surface defect size ($\sqrt{area_{R,max}}$) for AM250 annealed as-built surface specimens were calculated as 219 μm and 175 μm, respectively. $\sqrt{area_{R,max}}$ for machined surface specimens is considered zero as their surface roughness is less than 1 μm.

Considering that in most of the observed experimental cases the initiation of failure or the failure crack started at or very close to the surface, an equivalent semi-elliptical surface crack was assumed for fatigue life predictions. Also, the effect of defect shape is taken into account by considering various aspect ratios as an important representation for the initial defect shape (Fig. 18). This is due to the fact that irregular shape defects usually tend to transit quickly into an approximately smooth shape crack with various aspect ratios. Since the size of the surface defects is usually very small with respect to the diameter of the specimen, the local curvature of the specimen surface could be neglected.

The stress intensity correction factor for crack geometry suggested by Murakami for inclined semi-elliptical cracks [99] was used to take into account the aspect ratio and inclination angle of the defect. For vertically built specimens considered here, inclination angle of the crack is taken as zero because of the assumption that most of the defects are elongated between the layers and perpendicular to build direction. Using appropriate assumptions, the correction factor calculated based on the equation proposed by Newman and Raju [100] for finite thickness plate with a surface elliptical crack yielded approximately similar values for the same aspect ratios. The crack growth constants required for the life predictions were gathered from crack growth studies performed on similar AM Ti-6Al-4V in the literature [18,72].

6.2. Fatigue life modeling

A generalized Paris equation proposed by Pugno et al. [101] was adopted for prediction of the fatigue life. The aim of their method was to achieve an asymptotic match between the regime described by the Basquin equation and the regime described by the Paris equation. This can be interpreted as a Kitagawa-Takahashi method extended to finite life. Their rationale behind this asymptotic match was to avoid modeling of plasticity effect at a short crack tip. Quantized Fracture Mechanics was used to substitute the SIF, K, with a mean value:

$$K^* = \sigma\sqrt{(\pi(a + \Delta a/2))} \tag{5}$$

where σ is the applied remote stress and a is the crack length. Paris equation was used to relate the crack growth rate to the SIF range:

$$\frac{da}{dN} = C(\Delta K^*(a, \Delta a, \Delta\sigma))^n \tag{6}$$

where n and C are Paris equation constants which based on results for annealed LB-PBF Ti-6Al-4V alloy in literature [18] are taken as 3.92 and 3.18×10^{-12} m/cycle, respectively. In order to use this approach for the LB-PBF Ti-6Al-4V material, it was assumed that in the limiting case which the initial defect size tends to zero ($a_i \rightarrow 0$), the total fatigue life calculated from integration of Paris equation is equal to the prediction by the Basquin's equation for the wrought Ti-6Al-4V material. This implies that in an ideal case, where AM metal has a very similar microstructure and as a result crack initiation fatigue life to the wrought material, the only difference between the AM and wrought

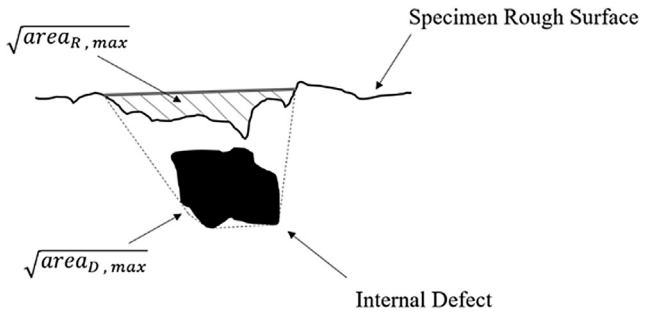

Fig. 17. Schematic representations of effective defect size [97].

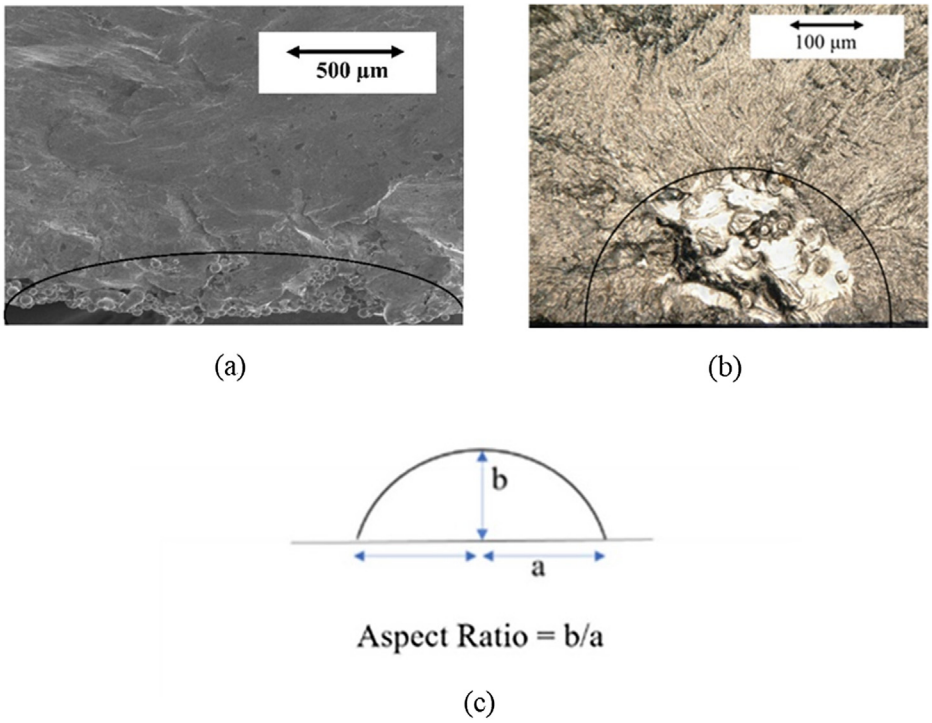

Fig. 18. (a) The effective area of a defect served as crack initiation site on the fracture surface of an as-built surface specimen, (b) the effective area of a near surface defect served as crack initiation site on the fracture surface of a machined surface specimen, and (c) schematic view of the aspect ratio.

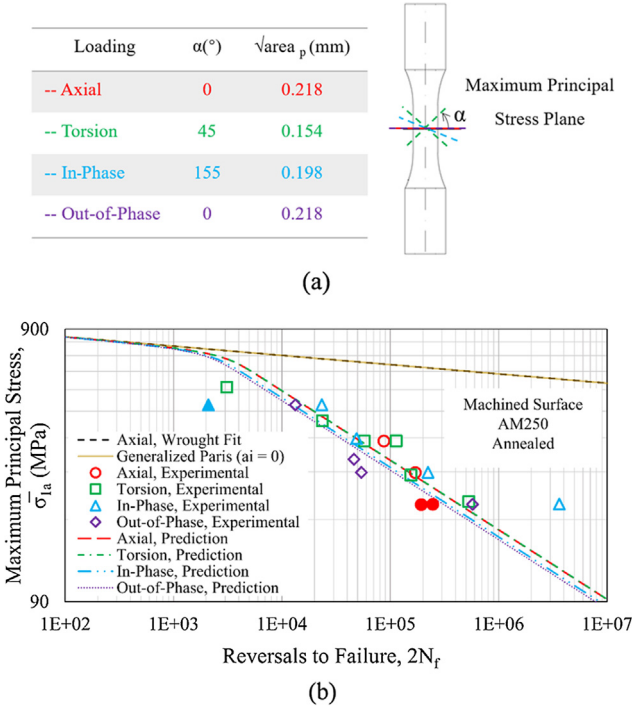

Fig. 19. (a) Projection of the defect size on the plane of maximum principal stress for each loading condition and, (b) experimental data and calculated fatigue curves (Aspect Ratio = 0.5) for different loading conditions of annealed LB-PBF Ti-6Al-4V with machined surface condition using generalized Paris equation. (Significantly large fabrication defects were found on the fracture surfaces corresponding to the solid data points).

materials is existence of defects and different crack growth properties. These assumptions, accompanied by considering that the effect of final crack length is negligible and taking the aspect ratio of the crack as constant throughout the propagation life, leads to the following equation for fatigue life:

$$N_f \cong \frac{1}{Y^n C \Delta\sigma^n \pi^{n/2}} \frac{\left[a_i + \left(\frac{\Delta\sigma^{-\frac{1}{b}-n}}{YCC^{'}\pi^{\frac{n}{2}}\left(\frac{n}{2}-1\right)}\right)^{\frac{1}{\frac{n}{2}-1}}\right]^{1-n/2}}{\frac{n}{2}-1} \quad (7)$$

where Y is the crack geometry factor for the case of inclined semi-elliptical cracks suggested by Murakami [99], and $C^{'}$ is calculated based on the Basquin equation constants of the wrought material:

$$C^{'} = 2(2\sigma^{'}_{f})^{1/b} \quad (8)$$

where $\sigma^{'}_{f} = 987$ MPa is the fatigue strength coefficient and $b = -0.034$ is the fatigue strength coefficient gathered from uniaxial fatigue testing of the wrought material [25]. For each loading scenario (i.e. axial, torsion, or combined loading), the initial defect size a_i, is substituted by the projection of the effective maximum prospective defect size ($\sqrt{area_p}$) calculated from EVS, on the plane which is experiencing the maximum principal stress and makes an angle α with the horizontal direction [99]:

$$\sqrt{area_p} = \sqrt{area_{eff,max}} \cdot \cos\alpha \quad (9)$$

6.3. Internal defects

For the AM250 LB-PBF Ti-6Al-4V specimens with large process-induced irregular shape defects and low ductility, crack initiation was observed on the plane of maximum principal stress and mode-I crack growth was dominant. For machined surface specimens the effective initial defect size $\sqrt{area_{eff,max}}$ was calculated based only on the size distribution of the internal defects since the measured surface roughness was not significant compared to the internal defects size (less than 1 µm). Fatigue test results and the predicted curves for vertically built annealed and machined surface LB-PBF Ti-6Al-4V specimens are shown in Fig. 19. The initial defect size used in fatigue life predictions

for each loading condition which was gathered from the EVS analysis of the 2D defect characterization results, is also shown in the figure.

The fatigue life prediction results presented in Fig. 19(b) are based on the aspect ratio of 0.5 which is a reasonable assumption based on the crack initiating defects observed on the fracture surfaces. The fatigue life prediction results based on maximum prospective defect size from EVS methods presented in Part I [1] of this paper series shows reasonable correlation with the experimental data, despite the discussion surround Fig. 2. As can be interpreted from Eq. (7), the prediction results are first very sensitive to the initial defect size and then sensitive to the aspect ratio of the initial defect. It can be observed from this figure that the axial and combined out-of-phase axial-torsion tested specimens generally showed slightly lower fatigue life for the same level of maximum principal stress, compared to torsion and combined in-phase axial-torsion tested specimens. This agrees well with the assumption to calculate the effective defect size observed for each loading condition as the projection of the maximum prospective defect size on the plane of maximum principal stress which is the lowest for torsion loading condition.

As mentioned earlier and based on the experimental observations, annealed specimens containing large defects generally showed tensile failure mode, while the HIPed material exhibited shear failure mode, which is similar to the failure mechanism of the wrought material. This is due to the difference in microstructure and defect characteristics inherent to the material and the fact that while the material is very sensitive to the presence of defects in as-built state and annealed condition, HIP treatment decreases this sensitivity. Fatigue life prediction methods and results for HIPed specimens with shear failure mode are currently under investigation by the authors.

6.4. Surface roughness

For as-built surface specimens the effective initial defect size was calculated based on the size distribution of the internal defects and the surface roughness profile as explained earlier. Fatigue test results and the predicted curves for annealed as-built surface LB-PBF Ti-6Al-4V specimens fabricated with AM250 are shown in Fig. 20. The fatigue life prediction results presented in this figure are based on the aspect ratio of 0.25, since a slenderer effective defect along the rough surface exits, as seen from Fig. 18(a), compared to the machined surface with aspect ratio of 0.5, as can be seen from Fig. 18(b). Changing the aspect ratio from 0.5 to 0.25, decreases the life prediction results about 40%. The data points shown as solid are associated with the specimens for which very large defects were observed on the fracture surfaces. These defects were significantly larger than the defects observed on the polished surfaces used for EVS and are considered outliers. They could be caused by manufacturing errors which are scarce and could be avoided, but these defects can be problematic for modeling the fatigue life based on the statistical analysis of the defect distribution.

7. Component fatigue testing and life predictions

Mechanical properties in general, and fatigue performance in particular, may differ from small laboratory specimens to the large component levels. This is due to the fact that additional factors at the component level often need to be considered, which are not typically considered at the laboratory coupon test level. These include stress concentration and gradient effects, size and scaling effects, joint and contact stresses, surface treatment and residual stresses, multiaxial and variable amplitude loadings, and environmental effects such as corrosion and temperature.

Such effects may be more significant for AM materials, where a change in the size or scale and orientation of the part and, therefore, thermal history, could result in different mechanical properties. In addition, presence of defects, both internal and surface, and their interactions with the stress concentrations and residual stresses can add more complexities to the task of performing accurate fatigue life prediction of AM components. Selection of a proper fatigue damage model could also significantly affect the bridging between coupon tests and component level fatigue performance predictions.

Although component fatigue testing can be expensive and time consuming, it is often necessary for fatigue life analysis validation. To demonstrate transferability of the coupon test data presented in the previous sections to component level fatigue life prediction, fatigue test results from an AM flight-critical nacelle link of an aircraft [102] were considered. The link was fabricated with the same type and model machine as M290 with default build parameters used for the fabrication process. Each build involved a set of four links as well solid cylindrical rods for machining specimens and testing as witness coupons. A representative of the build plate is shown in Fig. 21(a). After fabrication the links and witness coupons were subjected to a similar HIP treatment as in [6], but for 2 h, and subsequently machined to avoid any adverse effect of the rough surfaces.

Uniaxial load-controlled fatigue tests were performed on both the links and witness coupons. Coupon tests were performed under both $R = -1$ and $R = 0.1$ conditions, while 9 link tests were only done under fully-reversed $R = -1$ stress ratio. Representatives of the assembled link on the fatigue testing machine and fracture location sites are shown in Fig. 21(b)–(d). For more information about the testing procedures the reader is referred to [102]. While the specimens were built in vertical and diagonal orientations with respect to the build plate (discussed in previous sections), witness coupons were fabricated in horizontal (X, Y), and Z directions, as shown in Fig. 21(a). It is worth noting that although negligible or no anisotropy was observed for specimen tests fabricated in vertical and diagonal orientations after undergoing the HIP process, as discussed extensively in previous sections, a relatively large amount of anisotropy has been reported in [102] for the witness coupons. As can be seen in this figure, all of the link components are built in the horizontal direction.

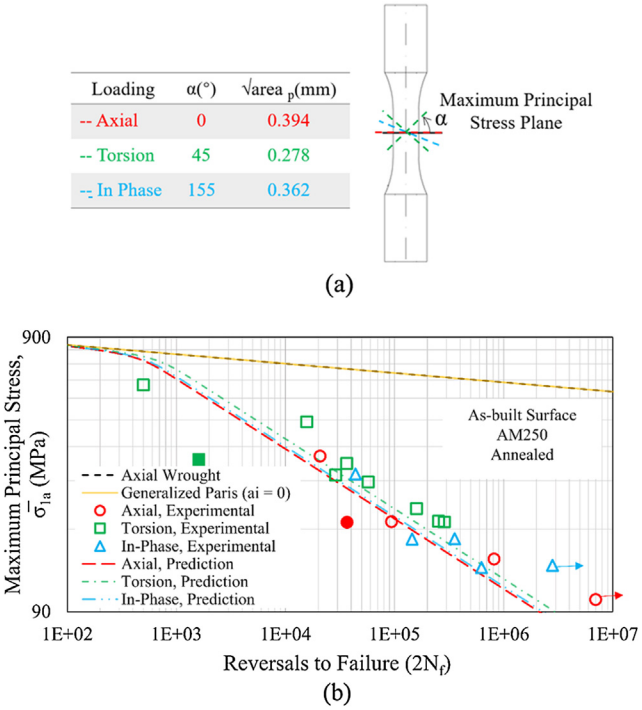

Fig. 20. (a) Projection of the defect size on the plane of maximum principal stress for each loading condition and, (b) experimental data and calculated fatigue curves (Aspect Ratio = 0.25) for different loading conditions of annealed LB-PBF Ti-6Al-4V with as-built surface condition using generalized Paris equation. (Significantly large fabrication defects were found on the fracture surfaces corresponding to the solid data points).

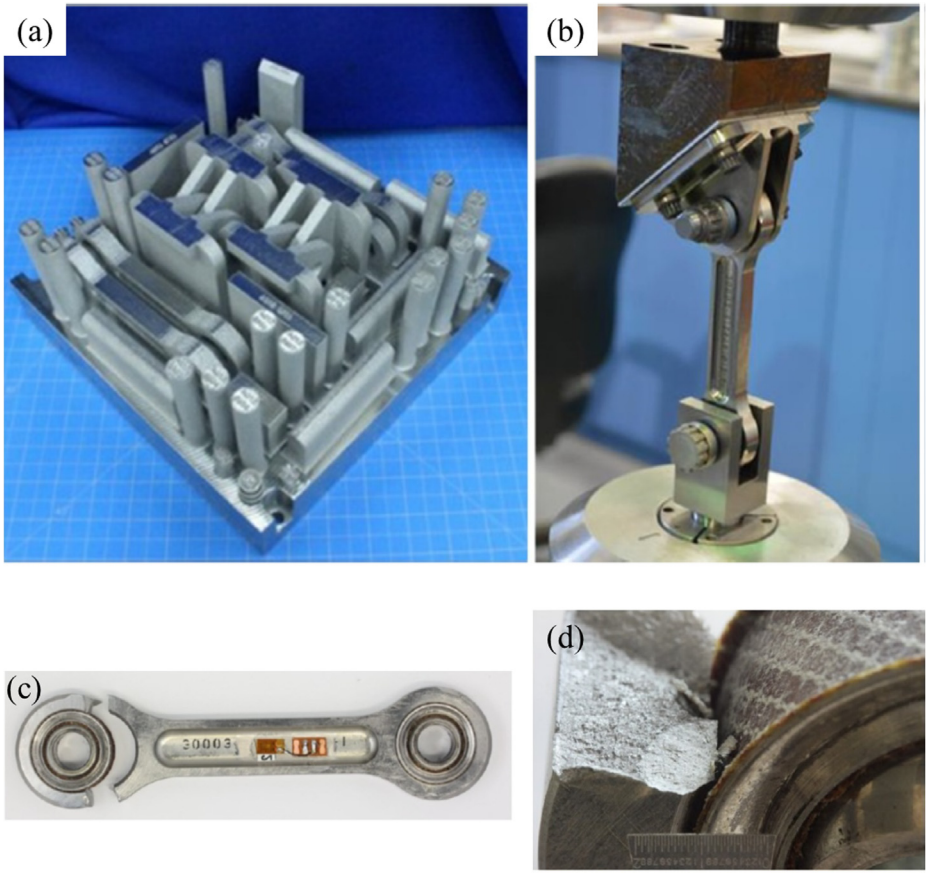

Fig. 21. (a) The layout of the build plate for the uniaxial specimens and V-22 links. (b) Axial fatigue test configuration of the link. (c) Representative of the fractured link assembly and, (d) crack initiation [102].

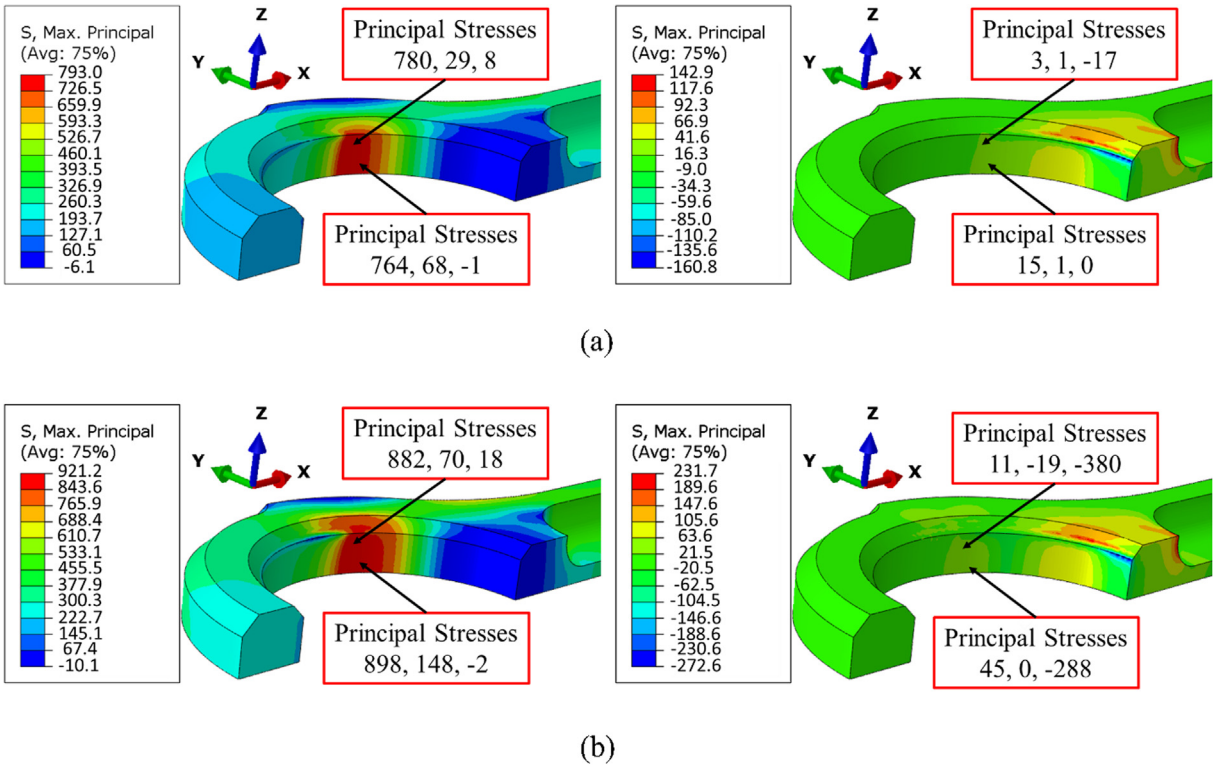

Fig. 22. Finite element results for one-eighth of the link during tension and compression load cycles with (a) nominal applied load amplitude of 31.14 kN (corresponding to 7000 lbs.), and (b) nominal applied load amplitude of 48.93 kN (corresponding to 11,000 lbs.).

The prediction of fatigue life involves two steps. First stresses and strains at fatigue critical location(s) need to be determined, in this case from FEA. Then, using the obtained stresses and strains in an appropriate fatigue damage model, the life can be predicted, as described in the following subsections.

7.1. Prediction of the stress field at the critical location of the link via FEA

The stress field in the link was obtained via the commercial Finite Element Analysis (FEA) tool, ABAQUS/Standard. The domain was discretized using 10-node tetrahedron elements with 4 integration points and quadratic shape functions (C3D10), with the element size of about 0.63 mm. Strains and rotations were approximated as infinitesimal and the solution was obtained via Newton's method. Considering the symmetry of both the link geometry and loading, only one eighth of the assembly was modeled to reduce the simulation time.

The fatigue tested assembly was simplified to be a pin with contact against the link. The load was applied through the pin using a surface to surface contact. To assess the interactions between the link and the pin, after considering several options, a rigid pin with a friction coefficient of 0.3 was chosen. The material properties were taken from [6], and an isotropic J2 yield model was used with an associative flow rule. Also, steady state cyclic stress-strain properties presented in [6] were used for the non-linear analysis.

It is worth mentioning that when the applied load transitions from tensile to compression, the associated nonlinearity of load transfer at the pin-link contact produces a very nonlinear load path in stress space at many locations. However, within the fatigue critical locations, the compressive applied load does not induce significant stresses. Hence, it can be concluded that the compressive part of the applied loading cycle does not have any effect on the fatigue life.

The finite element stress state results under two nominal fully-reversed uniaxial loads are shown in Fig. 22. As can be seen, the stress states at the highly stressed regions indicate presence of multiaxial stresses. This is not surprising, since presence of stress concentrations often result in multiaxial stress states, even under nominal uniaxial loadings [89]. In addition, the fully-reversed nature of the applied load does not result in fully-reversed stress ratio, $R = -1$, at the critical location of the link. For example, at a nominal applied load amplitude of 31.14 kN (see Fig. 22(a)), where there is little or no residual stresses at the critical location of the link, the stress ratio in the highly stressed region is approximately $R = 0$. However, at a higher nominal applied load amplitude of 48.93 kN (i.e. Fig. 22(b)), the stress ratio at the critical location is about $R = -0.5$ due to the presence of compressive residual stresses which occur due to the plastic deformation during the tensile portion of the loading.

As can be seen from Fig. 21, the finite element results are consistent with the representative fracture site of the link, suggesting that the fatigue failure occurred within the highly stressed region. However, in one of the 9 tests, the life governing fatigue crack initiated from the outer side of the link where the stress amplitude is substantially lower, which could be due to several factors such as machining marks or scratches on the surface.

7.2. Fatigue life predictions and data correlation

As discussed in Section 5.4, among different multiaxial fatigue predictive models, classical yield criteria such as von-Mises equivalent stress or strain are often used for the analysis, however, they lack a general robustness when the loading conditions become more complex. On the other hand, it was shown that critical plane-based approaches have the capability of reflecting the damage mechanisms of the material and are, hence, more robust.

It was shown in [6] that the Fatemi-Socie critical plane parameter [103] was consistent with the experimentally observed shear failure mechanism of the LB-PBF HIPed specimens under multiaxial stress states, resulting in satisfactory data correlations. Therefore, this parameter was used here to correlate the multiaxial specimen test results reported in [6], with those of the uniaxial witness coupon test results with different R ratios reported in [102] as well as with the fully-reversed link test results. A modified form of the parameter proposed by Gates and Fatemi [104] was used, given by:

$$\frac{\Delta\gamma_{max}}{2}\left(1 + k\frac{\sigma_{n,max}}{G\Delta\gamma}\right) = \frac{\tau_f^{'}}{G}(2N_f)^{b_0} + \gamma_f^{'}(2N_f)^{c_0} \tag{10}$$

where $\Delta\gamma$ is the shear strain range on the plane that experiences that maximum shear strain range, $\Delta\gamma_{max}$ is the maximum shear strain range experienced on the plane where the damage parameter is maximized, $\sigma_{n,max}$ is the maximum normal stress occurring on the plane where the damage parameter is maximized, G is the shear modulus, and k is the material dependent parameter which reflects the influence of normal stress on fatigue damage. The value of k was found to be 1.0 for the LB-PBF HIPed material. It was discussed in [104] that the modified damage parameter maintains all of the advantages and physical interpretations of the original FS parameter, while it better accounts for the effect of tensile mean stress.

Local stresses and strains were extracted from non-linear FEA results at the fatigue critical location, as discussed in the previous section, for input to the left side of Eq. (10). It is worth noting that although different approaches such as Theory of Critical Distance (TCD) are mostly being used in fatigue analysis of the notched members in the literature to account for the stress and/or strain gradient effects, this was not considered in this particular study for a number of reasons. First, due to the critical application of the link in an aircraft, this was done to consider the worst-case scenario and have a conservative fatigue life prediction. In addition, due to the geometry of the link, it could be assumed that the stress/strain gradient effect is negligible.

Fig. 23 shows that using this parameter results in a reasonably good correlation of the all the data, with the great majority of the data within ± 10% damage value scatter bands. These include specimen data under different stress states, witness coupon test data with or without mean stress (i.e. different R ratios), and the link data. However, as can be seen there is a relatively large scatter in witness coupon data which in some cases becomes as large as 6 orders of magnitude in fatigue life, in which could be due to several factors. For more information about the witness coupon and link component testing procedures the reader is referred to [102]. It is also worth noting that only the horizontally built witness coupon data are used in this figure. This was done due to the fact that the link components are built in horizontal orientation, and the orientation of their fatigue failure location is more

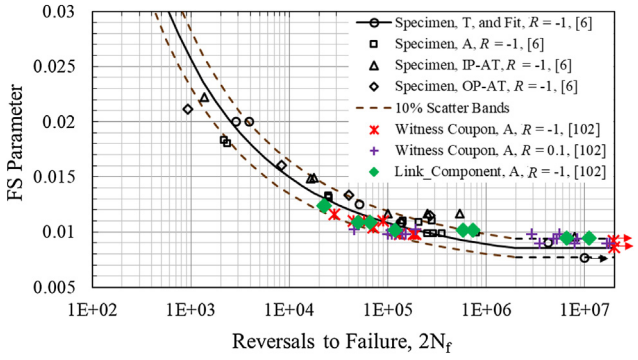

Fig. 23. Semi-log correlation of the multiaxial specimen test results (A: Axial; T: Torsion; IP-AT: Combined In-Phase Axial-Torsion; OP-AT: Combined 90° Out-of-Phase Axial-Torsion) reported in [6], with those of the uniaxial witness coupon test results reported in [102] with different R ratios as well as their uniaxial fully-reversed link assembly test results. All of the specimens, witness coupons, and link assembly components were tested in machined surface condition.

similar to those of the horizontal witness coupons.

Such results indicate promise in reasonable predictability of AM component fatigue performance based on test coupon fatigue data. It should, however, be noted that while the link used here included some key features of a representative component, it did not include some of the other complexities mentioned earlier, such as surface roughness, variable amplitude loading, or environmental aspects.

8. Summary and conclusions

In this Part II of the two-part paper series, uniaxial, torsion, and multiaxial fatigue behaviors of LB-PBF Ti-6Al-4V alloy were reviewed based on data generated by the authors and their relationships with microstructure and defect features were discussed (i.e. structure-property relationships). Despite the relatively large amount of uniaxial data for AM Ti-6Al-4V, there is very little information on this alloy with regards to torsion and multiaxial fatigue behaviors, in spite of their importance in many practical applications. Fatigue behavior of specimens fabricated with different fabrication systems and geometries, several heat treatments, different surface roughness conditions, and three build orientations were considered. The relationship between the microstructures and defects produced under these different conditions, extensively reviewed in Part I [1] of this paper series, and the fatigue behavior under the aforementioned loading conditions was presented and discussed. The specimen fatigue data and behaviors are then used for component fatigue life analysis and life predictions.

Based on the experimental results and discussions in this paper, and while considering the information and discussions presented in Part I [1] of this paper series, the following conclusions can be drawn:

(1) Additive manufacturing fabrication systems and variations in the associated build parameters significantly affect the produced microstructure and defects, as well as surface roughness and residual stresses, and consequently the fatigue damage mechanism and behavior.
(2) Under all loading conditions the AM Ti-6Al-4V without any further surface and/or thermal post processing treatment exhibited significantly shorter fatigue lives, as compared to the wrought material due to the microstructural differences, defects, residual stresses, and surface roughness.
(3) Surface machining in all loading conditions considerably improves the fatigue behavior, which is mainly due to the removal of surface defects and their stress concentration effects. However, the improvements are not as significant as expected for the conventionally fabricated wrought metals, which is due to the internal defects still present after rough surface removal.
(4) Selection of process parameters and/or post fabrication thermal processes such as HIPing, which acts to neutralize defects, may result in a reduction or elimination of anisotropic fatigue behavior.
(5) Selecting appropriate processing parameters and build orientations and/or post fabrication heat treatment processes could eliminate or significantly decrease residual stresses produced during the fabrication process, and therefore, their effects on fatigue performance.
(6) Proper thermo-mechanical HIP treatment can transform the martensitic microstructure to a microstructure similar to the wrought material with an $\alpha + \beta$ phase, neutralize defects, and relax of residual stresses. This, in turn, can elevate the fatigue performance to the same level as the wrought metal, when subsequent machining is performed.
(7) While defects have been shown to degrade the fatigue performance of additive manufactured Ti-6Al-4V, with lack of fusion defects often being the most detrimental, the fatigue strength is not only dependent on the defect size, but shape and location also play a significant role in the criticality of a given defect.
(8) The failure mechanism observed under different stress states depends on the microstructure, defect characteristics, and post surface and heat treatment processes utilized. Annealed specimens exhibited a tensile failure mode, while the HIPed specimens had a shear failure mode similar to the failure mode of the wrought material.
(9) Fatigue behavior under different loading conditions was dominated by microcracks occurring along specific plane orientations. Damage models consistent with the damage mechanisms and cracking orientations correlated the fatigue data under different stress states. This resulted in annealed specimen data correlating well with maximum principal stress criterion suited for tensile failure mode and the HIPed specimens data well correlating well with the Fatemi-Socie critical plane parameter suited for shear failure mode.
(10) Fatigue life predictions based on the maximum prospective effective defect size determined from EVS and calculated based on the maximum principal stress direction for each loading condition were reasonably close with 85% of the predicted lives within a scatter band of 3 as compared to the experimental fatigue lives for annealed as-built surface and machined surface specimens.
(11) With an appropriate fatigue damage model based on the physics of the damage process, fatigue performance of a component may be satisfactorily predicted based on the material fatigue behavior obtained from specimen fatigue tests.

Acknowledgment

United States Naval Air Systems Command (NAVAIR) provided partial financial support for this study. This material is also based upon work partially supported by the National Science Foundation (NSF) under Grant No. 1657195. DHW acknowledges financial support from ONR contract #N000141712035. S.S. acknowledges the help of Shahrior Ahmed with the collection of data for Figure 2, which was a part of his term project.

References

[1] Pegues J, Ahmed S, Shao S, Shamsaei N, Sanaei N, Fatemi A. Fatigue of additive manufactured Ti-6Al-4V. Part I: The effects of powder feedstock, manufacturing, and post process conditions on the resulting microstructure and defects. Int J Fatigue 2019 [Accepted Manuscript].
[2] Milne I, Ritchie RO, Karihaloo BL. Comprehensive structural integrity: Cyclic loading and fatigue. 2003; vol. 4: pp. 129-164.
[3] Stephens RI, Fatemi A, Stephens RR, Fuchs HO. Metal Fatigue in Engineering. 2nd Ed. John Wiley & Sons; 2000.
[4] Muralidharan U, Manson S. A modified universal slopes equation for estimation of fatigue characteristics of metals. J Eng Mater Technol 1988;110:55–8.
[5] Roessle M, Fatemi A. Strain-controlled fatigue properties of steels and some simple approximations. Int J Fatigue 2000;22:495–511.
[6] Molaei R, Fatemi A, Phan N. Significance of hot isostatic pressing (HIP) on multiaxial deformation and fatigue behaviors of additive manufactured Ti-6Al-4V including build orientation and surface roughness effects. Int J Fatigue 2018;117:352–70.
[7] Mower TM, Long MJ. Mechanical behavior of additive manufactured, powder-bed laser-fused materials. Mater Sci Eng, A 2016;651:198–213.
[8] Masuo H, Tanaka Y, Morokoshi S, Uchida T, Yamamoto Y, Murakami Y. Influence of defects, surface roughness and HIP on the fatigue strength of Ti-6Al-4V manufactured by additive manufacturing. Int J Fatigue 2018.
[9] Kobryn P, Semiatin S. Mechanical properties of laser-deposited Ti-6Al-4V. Solid Freeform Fabrication Proceedings; 2001. p. 6–8.
[10] Nicoletto G. Anisotropic high cycle fatigue behavior of Ti–6Al–4V obtained by powder bed laser fusion. Int J Fatigue 2017;94:255–62.
[11] Sterling AJ, Torries B, Shamsaei N, Thompson SM, Seely DW. Fatigue behavior and failure mechanisms of direct laser deposited Ti–6Al–4V. Mater Sci Eng, A 2016;655:100–12.
[12] Zhao X, Li S, Zhang M, Liu Y, Sercombe TB, Wang S, et al. Comparison of the microstructures and mechanical properties of Ti–6Al–4V fabricated by selective laser melting and electron beam melting. Mater Des 2016;95:21–31.
[13] Shui X, Yamanaka K, Mori M, Nagata Y, Kurita K, Chiba A. Effects of post-processing on cyclic fatigue response of a titanium alloy additively manufactured by electron beam melting. Mater Sci Eng, A 2017;680:239–48.
[14] Leuders S, Lieneke T, Lammers S, Tröster T, Niendorf T. On the fatigue properties of metals manufactured by selective laser melting –The role of ductility. J Mater

Res 2014;29:1911–9.
[15] Kasperovich G, Hausmann J. Improvement of fatigue resistance and ductility of Ti-6Al-4V processed by selective laser melting. J Mater Process Technol 2015;220:202–14.
[16] Wycisk E, Solbach A, Siddique S, Herzog D, Walther F, Emmelmann C. Effects of defects in laser additive manufactured Ti-6Al-4V on fatigue properties. Phys Procedia 2014;56:371–8.
[17] Rafi H, Karthik N, Gong H, Starr TL, Stucker BE. Microstructures and mechanical properties of Ti-6Al-4V parts fabricated by selective laser melting and electron beam melting. J Mater Eng Perform 2013;22:3872–83.
[18] Greitemeier D, Palm F, Syassen F, Melz T. Fatigue performance of additive manufactured Ti-6Al-4V using electron and laser beam melting. Int J Fatigue 2017;94:211–7.
[19] Hrabe N, Gnäupel-Herold T, Quinn T. Fatigue properties of a titanium alloy (Ti–6Al–4V) fabricated via electron beam melting (EBM): Effects of internal defects and residual stress. Int J Fatigue 2017;94:202–10.
[20] Kirchner A, Klöden B, Weißgärber T, Kieback B, Schoberth A, Bagehorn S, et al. Mechanical properties of Ti-6Al-4V additively manufactured by electron beam melting. Euro PM2015 Congress & Exhibition; 2014.
[21] Gong H. Generation and detection of defects in metallic parts fabricated by selective laser melting and electron beal melting and their effects on mechanical properties, PhD Thesis, University of Louisville; 2013.
[22] Li P, Warner D, Fatemi A, Phan N. Critical assessment of the fatigue performance of additively manufactured Ti–6Al–4V and perspective for future research. Int J Fatigue 2016;85:130–43.
[23] Fatemi A, Shamsaei N. Multiaxial fatigue: An overview and some approximation models for life estimation. Int J Fatigue 2011;33:948–58.
[24] Fatemi A, Molaei R, Sharifimehr S, Shamsaei N, Phan N. Torsional fatigue behavior of wrought and additive manufactured Ti-6Al-4V by powder bed fusion including surface finish effect. Int J Fatigue 2017;99:187–201.
[25] Fatemi A, Molaei R, Sharifimehr S, Phan N, Shamsaei N. Multiaxial fatigue behavior of wrought and additive manufactured Ti-6Al-4V including surface finish effect. Int J Fatigue 2017;100:347–66.
[26] Murakami Y, Beretta S. Small defects and inhomogeneities in fatigue strength: experiments, models and statistical implications. Extremes 1999;2:123–47.
[27] Romano S, Brückner-Foit A, Brandão A, Gumpinger J, Ghidini T, Beretta S. Fatigue properties of AlSi10Mg obtained by additive manufacturing: Defect-based modelling and prediction of fatigue strength. Eng Fract Mech 2018;187:165–89.
[28] Yadollahi A, Shamsaei N. Additive manufacturing of fatigue resistant materials: Challenges and opportunities. Int J Fatigue 2017;98:14–31.
[29] Seifi M, Gorelik M, Waller J, Hrabe N, Shamsaei N, Daniewicz S, et al. Progress towards metal additive manufacturing standardization to support qualification and certification. J Miner, Met Mater Soc 2017;69:439–55.
[30] ASTM-B348-13. Standard specification for titanium and titanium alloy bars and billets. Annual Book of ASTM Standards, vol. 02.04; 2013.
[31] ASTM-E2207-15. Standard practice for strain-controlled axial-torsional fatigue testing with thin-walled tubular specimens. Annual Book of ASTM Standards, vol. 03.01; 2015.
[32] Torries B, Shamsaei N, Thompson SM. Effects of build orientation on fatigue performance of Ti-6Al-4V parts fabricated via laser-based powder bed fusion. In: 28th International Solid Freeform Fabrication Symposium-An Additive Manufacturing Conference; 2017.
[33] ASTM-F2924-14. Standard specification for additive manufacturing Titanium-6 Aluminum-4 Vanadium with powder bed fusion. Annual Book of ASTM Standards, vol. 10.04; 2014.
[34] Chawla KK, Meyers M. Mechanical behavior of materials; 1999.
[35] Tofique MW, Bergström J, Burman C. Very high cycle fatigue crack initiation mechanisms in different engineering alloys. Procedia Struct Integrity 2016;2:1181–90.
[36] Kazymyrovych V, Bergström J, Burman C. The significance of crack initiation stage in very high cycle fatigue of steels. Steel Res Int 2010;81:308–14.
[37] Shao S, Khonsari MM, Wang J, Shamsaei N, Li N. Frequency dependent deformation reversibility during cyclic loading. Mater Res Lett 2018;6:390–7.
[38] Mughrabi H. Dislocation wall and cell structures and long-range internal stresses in deformed metal crystals. Acta Metall 1983;31:1367–79.
[39] Winter A. A model for the fatigue of copper at low plastic strain amplitudes. Phil Mag 1974;30:719–38.
[40] Finney J, Laird C. Strain localization in cyclic deformation of copper single crystals. Phil Mag 1975;31:339–66.
[41] Sangid MD, Ezaz T, Sehitoglu H, Robertson IM. Energy of slip transmission and nucleation at grain boundaries. Acta Mater 2011;59:283–96.
[42] Hall J. Fatigue crack initiation in alpha-beta titanium alloys. Int J Fatigue 1997;19:23–37.
[43] Bridier F, Villechaise P, Mendez J. Slip and fatigue crack formation processes in an α/β titanium alloy in relation to crystallographic texture on different scales. Acta Mater 2008;56:3951–62.
[44] Yadollahi A, Shamsaei N, Thompson SM, Seely DW. Effects of process time interval and heat treatment on the mechanical and microstructural properties of direct laser deposited 316L stainless steel. Mater Sci Eng, A 2015;644:171–83.
[45] Jiang R, Bull D, Evangelou A, Harte A, Pierron F, Sinclair I, et al. Strain accumulation and fatigue crack initiation at pores and carbides in a SX superalloy at room temperature. Int J Fatigue 2018;114:22–33.
[46] Tanaka K, Mura T. A dislocation model for fatigue crack initiation. J Appl Mech 1981;48:97–103.
[47] Sangid MD. The physics of fatigue crack initiation. Int J Fatigue 2013;57:58–72.
[48] Chan KS. Roles of microstructure in fatigue crack initiation. Int J Fatigue 2010;32:1428–47.
[49] Tanaka K, Mura T. A theory of fatigue crack initiation at inclusions. Metall Trans A 1982;13:117–23.
[50] Gong H, Rafi K, Gu H, Ram GJ, Starr T, Stucker B. Influence of defects on mechanical properties of Ti–6Al–4V components produced by selective laser melting and electron beam melting. Mater Des 2015;86:545–54.
[51] Edwards P, Ramulu M. Fatigue performance evaluation of selective laser melted Ti–6Al–4V. Mater Sci Eng, A 2014;598:327–37.
[52] Popov V, Katz-Demyanetz A, Garkun A, Muller G, Strokin E, Rosenson H. Effect of hot isostatic pressure treatment on the electron-beam melted Ti-6Al-4V specimens. Procedia Manuf 2018;21:125–32.
[53] Nalla R, Ritchie R, Boyce B, Campbell J, Peters J. Influence of microstructure on high-cycle fatigue of Ti-6Al-4V: bimodal vs. lamellar structures. Metall Mater Trans A 2002;33:899–918.
[54] Günther J, Krewerth D, Lippmann T, Leuders S, Tröster T, Weidner A, et al. Fatigue life of additively manufactured Ti–6Al–4V in the very high cycle fatigue regime. Int J Fatigue 2017;94:236–45.
[55] Zuo J, Wang Z, Han E. Effect of microstructure on ultra-high cycle fatigue behavior of Ti–6Al–4V. Mater Sci Eng, A 2008;473:147–52.
[56] Torries B, Shamsaei N. Fatigue behavior and modeling of additively manufactured Ti-6Al-4V including interlayer time interval effects. JOM 2017;69:2698–705.
[57] Liu QC, Elambasseril J, Sun SJ, Leary M, Brandt M, Sharp PK. The effect of manufacturing defects on the fatigue behaviour of Ti-6Al-4V specimens fabricated using selective laser melting. Adv Mater Res 2014;891:1519–24.
[58] Oh J, Lee JG, Kim NJ, Lee S, Lee EW. Effects of thickness on fatigue properties of investment cast Ti-6Al-4V alloy plates. J Mater Sci 2004;39:587–91.
[59] Lin C-W, Ju C-P, Lin J-HC. A comparison of the fatigue behavior of cast Ti–7.5 Mo with cp titanium, Ti–6Al–4V and Ti–13Nb–13Zr alloys. Biomaterials 2005;26:2899–907.
[60] Walker K. The effect of stress ratio during crack propagation and fatigue for 2024-T3 and 7075-T6 aluminum. Effects of Environment and Complex Load History on Fatigue Life; 1970.
[61] Li P, Warner D, Pegues J, Roach M, Shamsaei N, Phan N. Investigation of the mechanisms by which hot isostatic pressing improves the fatigue performance of powder bed fused Ti-6Al-4V. Int J Fatigue 2019;120:342–52.
[62] Carroll BE, Palmer TA, Beese AM. Anisotropic tensile behavior of Ti–6Al–4V components fabricated with directed energy deposition additive manufacturing. Acta Mater 2015;87:309–20.
[63] Chastand V, Tezenas A, Cadoret Y, Quaegebeur P, Maia W, Charkaluk E. Fatigue characterization of titanium Ti-6Al-4V samples produced by additive manufacturing. Procedia Struct Integrity 2016;2:3168–76.
[64] Gockel J, Beuth J, Taminger K. Integrated control of solidification microstructure and melt pool dimensions in electron beam wire feed additive manufacturing of Ti-6Al-4V. Addit Manuf 2014;1:119–26.
[65] Pegues J, Roach M, Williamson RS, Shamsaei N. Surface roughness effects on the fatigue strength of additively manufactured Ti-6Al-4V. Int J Fatigue 2018;116:543–52.
[66] Simonelli M, Tse Y, Tuck C. Effect of the build orientation on the mechanical properties and fracture modes of SLM Ti–6Al–4V. Mater Sci Eng, A 2014;616:1–11.
[67] Qiu C, Adkins NJ, Attallah MM. Microstructure and tensile properties of selectively laser-melted and of HIPed laser-melted Ti–6Al–4V. Mater Sci Eng, A 2013;578:230–9.
[68] Yadollahi A, Shamsaei N, Thompson SM, Elwany A, Bian L. Effects of building orientation and heat treatment on fatigue behavior of selective laser melted 17–4 PH stainless steel. Int J Fatigue 2016;94:218–35.
[69] Shrestha R, Simsiriwong J, Shamsaei N, Thompson SM, Bian L. Effect of build orientation on the fatigue behavior of stainless steel 316L manufactured via a laser-powder bed fusion process. In: 27th Annual Solid Frefform Fabrication Symposium Proceedings; 2016. p. 605–16.
[70] Fatemi A, Molaei R, Simsiriwong J, Sanaei N, Pegues J, Torries B, et al. Fatigue behavior of additive manufactured materials: An overview of some recent experimental data for Ti-6Al-4V considering various processing and loading direction effects. Fatigue Fract Eng Mater Struct 2019;42:991–1009.
[71] Wu M-W, Lai P-H. The positive effect of hot isostatic pressing on improving the anisotropies of bending and impact properties in selective laser melted Ti-6Al-4V alloy. Mater Sci Eng, A 2016;658:429–38.
[72] Leuders S, Thöne M, Riemer A, Niendorf T, Tröster T, Richard H, et al. On the mechanical behaviour of titanium alloy Ti-6Al-4V manufactured by selective laser melting: Fatigue resistance and crack growth performance. Int J Fatigue 2013;48:300–7.
[73] Vrancken B, Cain V, Knutsen R, Van Humbeeck J. Residual stress via the contour method in compact tension specimens produced via selective laser melting. Scr Mater 2014;87:29–32.
[74] Benedetti M, Torresani E, Leoni M, Fontanari V, Bandini M, Pederzolli C, et al. The effect of post-sintering treatments on the fatigue and biological behavior of Ti-6Al-4V ELI parts made by selective laser melting. J Mech Behav Biomed Mater 2017;71:295–306.
[75] Ali H, Ghadbeigi H, Mumtaz K. Effect of scanning strategies on residual stress and mechanical properties of Selective Laser Melted Ti-6Al-4V. Mater Sci Eng, A 2018;712:175–87.
[76] Parry L, Ashcroft I, Wildman RD. Understanding the effect of laser scan strategy on residual stress in selective laser melting through thermo-mechanical simulation. Addit Manuf 2016;12:1–15.
[77] Casavola C, Campanelli S, Pappalettere C. Experimental analysis of residual stresses in the selective laser melting process. In: Proccedings of the XIth International Congress and Exposition, Orlando, Florida, USA; 2008.

[78] Torries B, Shao S, Shamsaei N, Thompson SM. Effect of inter-layer time interval on the mechanical behavior of direct laser deposited Ti-6Al-4V. Solid Freeform Fabrication Symposium; 2016.
[79] Wu S, Lu Y, Gan Y, Huang T, Zhao C, Lin J, et al. Microstructural evolution and microhardness of a selective-laser-melted Ti–6Al–4V alloy after post heat treatments. J Alloy Compd 2016;672:643–52.
[80] Vilaro T, Colin C, Bartout J-D. As-fabricated and heat-treated microstructures of the Ti-6Al-4V alloy processed by selective laser melting. Metall Mater Trans A 2011;42:3190–9.
[81] Brandl E, Greitemeier D. Microstructure of additive layer manufactured Ti–6Al–4V after exceptional post heat treatments. Mater Lett 2012;81:84–7.
[82] Ter Haar G, Becker T. Selective laser melting produced Ti-6Al-4V: Post-process heat treatments to achieve superior tensile properties. Materials 2018;11:146.
[83] ASTM-F1472-14. Standard specification for wrought Titanium-6Aluminum-4Vanadium alloy for surgical implant applications (UNS R56400). Annual Book of ASTM Standards, vol. 13.01; 2014.
[84] Chan KS, Koike M, Mason RL, Okabe T. Fatigue life of titanium alloys fabricated by additive layer manufacturing techniques for dental implants. Metall Mater Trans A 2013;44:1010–22.
[85] Torries B, Imandoust A, Beretta S, Shao S, Shamsaei N. Overview on microstructure and defect sensitive fatigue modeling of additively manufactured materials. J Miner, Met Mater Soc 2018;70:1853–62.
[86] Greitemeier D, Dalle Donne C, Syassen F, Eufinger J, Melz T. Effect of surface roughness on fatigue performance of additive manufactured Ti-6Al-4V. Mater Sci Technol 2015;32:629–34.
[87] Pegues JW, Shamsaei N, Roach MD, Williamson RS. Fatigue life estimation of additive manufactured parts in the as-built surface condition. Mater Des Process Commun 2019:e36.
[88] Fatemi A, Molaei R, Sharifimehr S, Shamsaei N, Phan N. Torsional fatigue behaviour of wrought and selective laser melted Ti-6Al-4V including as-built and machined surface finish effects. In: 17th Australian International Aerospace Congress: AIAC 2017; 2017. p. 121.
[89] Molaei R, Fatemi A. Crack paths in additive manufactured metallic materials subjected to multiaxial cyclic loads including surface roughness, HIP, and notch effects. Int J Fatigue 2019;124:558–70.
[90] Masuo H, Tanaka Y, Morokoshi S, Yagura H, Uchida T, Yamamoto Y, et al. Effects of defects, surface roughness and HIP on fatigue strength of Ti-6Al-4V manufactured by additive manufacturing. Procedia Struct Integrity 2017;7:19–26.
[91] Gates N, Fatemi A. Friction and roughness induced closure effects on shear-mode crack growth and branching mechanisms. Int J Fatigue 2016;92:442–58.
[92] Shamsaei N, Fatemi A. Small fatigue crack growth under multiaxial stresses. Int J Fatigue 2014;58:126–35.
[93] Carrion P, Imandoust A, Simsiriwong J, Shamsaei N. Multiaxial fatigue behavior of additive manufactured Ti-6Al-4V. In: 29th Annual International Solid Freeform Fabrication Symposium Proceeding, TX; 2018.
[94] Molaei R, Fatemi A. Crack paths in additive manufactured Ti-6Al-4V specimens subjected to multiaxial cyclic loads. In: 6th International Conference on Crack Paths (CP 2018), Italy, September, 2018.
[95] Murakami Y, Kodama S, Konuma S. Quantitative evaluation of effects of non-metallic inclusions on fatigue strength of high strength steels. I: Basic fatigue mechanism and evaluation of correlation between the fatigue fracture stress and the size and location of non-metallic inclusions. Int J Fatigue 1989;11:291–8.
[96] Murakami Y. Inclusion rating by statistics of extreme values and its application to fatigue strength prediction and quality control of materials. J Res-Natl Instit Standards Technol 1994;99:345.
[97] Yamabe J, Kobayashi M. Influence of casting surfaces on fatigue strength of ductile cast iron. Fatigue Fract Eng Mater Struct 2006;29:403–15.
[98] Murakami Y, Takahashi K, Yamashita T. Quantitative evaluation of the effect of surface roughness on fatigue strength (Effect of depth and pitch of roughness). Nippon Kikai Gakkai Ronbunshu, A Hen/Trans Jpn Soc Mech Eng, Part A 1997;63:1612–9.
[99] Murakami Y. Analysis of stress intensity factors of modes I, II and III for inclined surface cracks of arbitrary shape. Eng Fract Mech 1985;22:101–14.
[100] Newman J, Raju I. Stress-intensity factor equations for cracks in three-dimensional finite bodies. In: Fracture Mechanics: Fourteenth Symposium—Volume I: Theory and Analysis; 1983.
[101] Pugno N, Ciavarella M, Cornetti P, Carpinteri A. A generalized Paris' law for fatigue crack growth. J Mech Phys Solids 2006;54:1333–49.
[102] Kasprzak JM, Lass AB, Miller CE. Development, test, and evaluation of additively manufactured flight critical aircraft components. In: AHS International 73rd Annual Forum & Technology Display, TX; 2017.
[103] Fatemi A, Socie DF. A Critical plane approach to multiaxial fatigue damage including out-of-phase loading. Fatigue Fract Eng Mater Struct 1988;11:149–65.
[104] Gates NR, Fatemi A. On the consideration of normal and shear stress interaction in multiaxial fatigue damage analysis. Int J Fatigue 2017;100:322–36.